



# Underwater noise

*"An analysis to the relevant criteria for positioning a bubble curtain."*

  
**TU Delft**

**Van Oord**   
Marine ingenuity

Govert Jan Glasbergen  
4700872  
MSc Offshore and dredging engineering

23-10-2020



# Underwater noise mitigation

*An analysis to the relevant criteria for positioning a bubble curtain.*

by

G.J.W. Glasbergen

to obtain the degree of  
**Master of Science**

in Offshore Engineering at the Delft University of Technology,  
to be defended publicly on October 23, 2020



Student number: 4700872  
Project duration: November 11, 2019 - October 23, 2020  
Thesis committee: Prof. Dr. A.V. Metrikine, TU Delft, Chair  
Dr. Ir. A. Tsouvalas, TU Delft, supervisor  
Dr. MSc. G. J. de Boer, Van Oord, supervisor  
MSc. P. J. Elzinga, Van Oord  
MSc. A. Stampoultzoglou, Van Oord

An electronic version of this thesis is available at  
<http://repository.tudelft.nl/>.



# Executive summary

Offshore wind farms are becoming more important with the growing demand for the new renewable energy (Ramirez et al., 2020). To raise the capacity of the Offshore Wind Farms (OWF), Offshore Wind Turbine Generators (OWTG) and their foundations are increasing in size. The most popular foundation concept is the monopile for which most common installation method is impact piling. The hammer strikes the monopile into the soil with hammer loads varying between 200-400 tonnes. The noise intensity that is released from the blow of the hammer can easily exceed peak pressures of more than 200 dB re 1  $\mu Pa$  (Elzinga et al., 2019). This brings harm to the aquatic environment and exceeds the noise limits demanded by governments leading to severe delays in construction.

This research focuses on the critical parameters that determine the location of a bubble curtain. This is done by using the semi-analytical SILENCE model (Tsovalas, 2015). It is compared to data obtained at the [REDACTED]. After validation of the model for the unmitigated case, a bubble curtain is modelled to assess the effects of different bubble curtain locations.

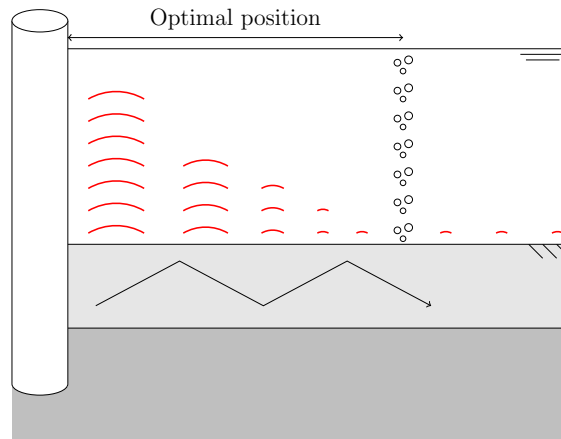
## Model

In this research the SILENCE model, developed at TU Delft is used. The SILENCE model is a second generation model. This means it takes soil effects like shear waves into account unlike other models who model the soil as an equivalent fluid. It is also a computationally fast model. This makes it ideal for doing parametric studies to learn more about the physics of underwater noise.

The model consists of a noise generation module and noise propagation module. The generation module generates a source in the vicinity of the pile. This source is subsequently propagated to further distances with the propagation module. With the propagation module, noise predictions at the legally required 750m can be made. Larger distances can also be calculated with limited computational power with a precision of  $\pm 2$  dB.

## Results and recommendations

The results of this research indicate that the noise in upper layer of the soil leaks back into the water column as sketched in the figure below. This leakage decays over radial distance. The frequency content of leakage is mainly shifted towards low frequencies ( $\approx 31.5\text{Hz}$ ).



Schematic overview of energy leakage

By placing the bubble curtain further away up to a certain distance ( $70\text{m} - 90\text{m}$ ) more noise reduction is achieved. If the bubble curtain is placed further away from the pile, no difference in reduction was observed. This is approximately the location up to which the energy leakage is significant. This noise leakage can be reduced by damping specifically to low frequencies. However, such a system needs to be placed far enough from the pile otherwise too much noise will travel underneath such a system.

Based on the results of this research the following recommendations are given:

- It is shown that energy leakage takes place up to a certain distance. It is recommended to look what the effect of different soil types is on the distance and frequency content of this leakage. For this, the SILENCE model is very suitable due to its computational efficiency.
- Based on full waterborne-path block simulations, there is still noise recorded in the simulation. It is thus shown that noise leakage is underestimated and contributes significantly to underwater noise emissions.
- It was shown that the noise reduction potential of a bubble curtain was lower compared to a full block. This is because the energy leakage is mainly shifted towards low frequencies. It is recommended to verify this by experiments.
- It was shown that the energy leakage is significant up to  $70\text{m}$ . It is debatable whether near-field noise mitigation systems are used for their full potential when placed in the vicinity of the pile.
- SILENCE belongs to the state of the art models which describe the physics in the soil in a correct way. The computational efficiency makes it possible to do extensive parametric studies. It was also able to calculate the noise limits within  $\pm 2\text{ dB}$  accuracy. However, it requires specialist knowledge to operate.

# Preface

Before you lies the work which, in addition to completing my MSc Offshore Engineering, sums up for me the past three years of academic education at TU Delft. Underwater noise, specifically to offshore piledriving, covers topics such as structural dynamics, wave mechanics and computational modeling. Subjects I loved the most from my study in Offshore Engineering.

This thesis comprises how noise travels through a soil-water domain and a model is proposed to determine an effective location of a Bubble Curtain. In a broad way, the ultimate goal is to place offshore renewables in a sustainable manner. I hope this thesis contributes to that goal.

I would like to take the opportunity to thank the people who were involved in this thesis. First, I would like to thank Prof. Dr. Andrei Metrikine and Dr. Apostolos Tsouvalas for their guidance, support and motivating advice. Secondly, I would like to thank Yaxi Peng. The weekly discussions we had were both educational and motivating. You helped me understand the SILENCE model and made me a more critical thinker. Your work was a large contribution to my thesis for which I thank you sincerely. Thirdly, I would like to thank Van Oord for the opportunity they gave me to research this topic within this company. I like to thank my supervisors especially for their involvement. Gerben, your practical mindset and love for programming amplified my interest in programming and data analysis. Jesper, through your practical mindset I learned to zoom out from the academic side of this thesis. It has helped me to give practical value to my research. Tasos, your enthusiasm has helped me to see the value of my findings. You always gave me a motivating spirit when we had a discussion.

I would like to finalize with great gratitude to my parents. You gave me the chance to develop myself and find a passion of which this thesis is a final result. I thank you deeply for the opportunity you gave me. And lastly Nicolien, I thank you for always supporting me.

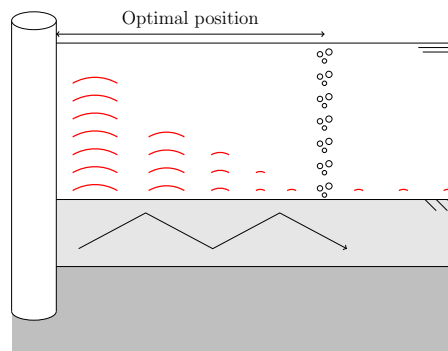
I enjoyed working on this thesis, I hope you enjoy reading it.

Govert Jan W. Glasbergen  
The Hague, October 23, 2020



# Abstract

Wind turbines are growing in size and therefore their foundations, become larger as well. Additionally, they are placed in deeper waters. This results in the industry being at the limit of underwater noise levels generated by impact piling during the installation phase of monopiles. The most common installation method for monopiles is impact piling. This installation method comes with high impulse noise emissions which can be harmful for the aquatic environment. Larger piles require more energetic hammer impacts which, in turn, generate more noise. Given the size of the monopiles installed nowadays, noise limits imposed by governmental organisations are exceeded in all cases. The noise due to impact piling can be reduced by applying noise mitigation measures. Several systems have been developed, the most common of which is the Big Bubble Curtain (BBC). Although the working principle of the BBC has been proven in practice, the most effective deployment configuration, i.e. distance from the pile, air-flow volume and pressure, etc., has not been thoroughly investigated. In current projects, the BBC is typically placed at twice the water depth. This study aims to identify the parameters that determine the optimum position of the BBC to achieve maximum noise reduction. First, free-field predictions (without the BBC) using the TU Delft software SILENCE have been carried out for model validation purposes. The accuracy of the noise predictions were found to be within 2 dB (re  $1\mu$  Pa) both for the SEL and the  $L_{p,pk}$ . Second, the BBC was implemented by assuming a depth and frequency-dependent transmission loss (TL) factor at the position of the BBC. Noise predictions including the modelling of the BBC were validated against measured data. The key findings in this research are that the location of the bubble curtain is determined by the energy leakage from the soil into the water column. Depending on the damping characteristics of the BBC, this leakage is significant up to a point where the energy does not leak back to the water column anymore. In the examined case, and for blocking the waterborne path, this optimal position is found to be around 70m. The figure below shows the trend of the energy leakage in a schematic way. It shows that if the bubble curtain is placed too close to the pile, noise leaks back into the water column behind the bubble curtain. Thus, depending on the specific geometrical configuration, water depth and soil conditions, it is argued that an optimum position can always be found using the analysis presented in this work.



The influence of energy leakage to the location of the bubble curtain



# Contents

List of Figures

List of Tables

List of Abbreviations

Nomenclature

<b>1</b>	<b>Introduction</b>	<b>1</b>
1.1	Scope . . . . .	2
1.1.1	Approach . . . . .	3
1.2	Thesis outline . . . . .	4
<b>2</b>	<b>Theoretical background</b>	<b>5</b>
2.1	Acoustic fundamentals . . . . .	5
2.1.1	Acoustic quantities . . . . .	6
2.1.2	The decibel scale . . . . .	8
2.1.3	The Helmholtz equation . . . . .	8
2.2	The sources of noise . . . . .	9
2.2.1	Hammer impact . . . . .	9
2.2.2	Pile response . . . . .	9
2.2.3	Surface waves . . . . .	11
2.2.4	Seismic waves . . . . .	12
2.3	State of the art noise mitigation techniques . . . . .	12
2.3.1	Single and Double Big Bubble curtains (BBC and DBBC) . . . . .	12
2.3.2	Small Bubble Curtain (SBC) . . . . .	13
2.3.3	Hydro Sound Damper (HSD) . . . . .	13
2.3.4	Noise mitigation screen (IHC-NMS) . . . . .	14
2.3.5	Cofferdam . . . . .	14
2.3.6	AdBm . . . . .	14
2.4	Noise prediction models . . . . .	14
2.5	Bubble curtain models . . . . .	15
<b>3</b>	<b>Modeling underwater noise</b>	<b>17</b>
3.1	Moving point source model . . . . .	17
3.1.1	Mathematical derivation . . . . .	17
3.1.2	Isovelocity problem . . . . .	19
3.2	SILENCE Near field model . . . . .	21
3.2.1	Pile . . . . .	22

3.2.2	Fluid domain . . . . .	23
3.2.3	Soil domain . . . . .	23
3.2.4	Boundary and interface conditions . . . . .	24
3.3	SILENCE Far field model . . . . .	25
3.4	Validation of the model . . . . .	27
3.4.1	Dataset . . . . .	27
3.4.2	Model input data . . . . .	29
3.4.3	Validation results . . . . .	34
3.4.4	Energy and spectra near the seabed . . . . .	38
<b>4</b>	<b>Bubble curtain implementation</b>	<b>41</b>
4.1	The noise reduction by a bubble curtain . . . . .	41
4.1.1	Noise reduction mechanisms . . . . .	41
4.1.2	The influence of currents . . . . .	42
4.1.3	Distance of the bubble curtain . . . . .	42
4.2	The effective source reduction approach . . . . .	43
4.3	Depth-dependent wavenumber . . . . .	44
4.4	Bubble curtain scenario's . . . . .	48
4.5	Bubble curtain validation results . . . . .	50
<b>5</b>	<b>The location of the bubble curtain</b>	<b>51</b>
5.1	Methodology of the parametric study . . . . .	51
5.2	Result of the parametric study . . . . .	51
5.3	Relation of the tipping point to the energy leakage . . . . .	52
5.4	Trend of the noise reduction potential . . . . .	54
5.5	Model flaws . . . . .	54
<b>6</b>	<b>Conclusion and recommendations</b>	<b>55</b>
6.1	Discussion and concluding remarks . . . . .	55
6.2	Recommendations . . . . .	57
	<b>Bibliography</b>	<b>59</b>
	<b>Appendix</b>	<b>63</b>
A	Bathymetry . . . . .	63
B	Zoom in of parametric study on bubble curtain location . . . . .	64
C	Sensitivity analysis for different bubble curtain configurations . . . . .	65
D	Notebooks . . . . .	69

# List of Figures

2.1	An example of a pressure recording in time (Bellmann, 2019) . . . . .	7
2.2	Processes of noise during offshore piling . . . . .	9
2.3	Compression strain wave in the pile (Kuhn et al., 2014) . . . . .	10
2.4	Chain of events of the Mach cone generation during a hammer blow, showing the different angles, wave speeds and direction of propagation. Figure (a) and (b) show the wave front going into the sediment. Note that the angle of the Mach cone changes. Figure (c) and (d) show the reflected waves traveling upward back into the watercolumn (Reinhall and Dahl, 2011). . . . .	11
2.5	Resultant wave fronts after reflection in the pile (Reinhall and Dahl, 2011) . . . . .	11
2.6	S-waves and P-waves (Britannica, 2020) . . . . .	12
2.7	The working principle of bubble curtains. . . . .	13
2.8	Schematic representation of HSD (Elmer and Savery, 2014) . . . . .	13
2.9	Mach wave radiation (Reinhall and Dahl, 2011) . . . . .	15
3.1	The isovelocity problem (Jensen et al., 2011) . . . . .	19
3.2	Pressure field time domain solution to the isovelocity problem . . . . .	21
3.3	Mach cone by moving a point source in time . . . . .	21
3.4	SILENCE Near-Field model geometry (Tsouvalas, 2015) . . . . .	22
3.5	Ring source in cylindrical coordinates (Tsouvalas, 2020) . . . . .	26
3.6	Schematic top overview of the measurement set-up (Elzinga et al., 2019) . . . . .	28
3.7	Force approximation based on the work of Lippert, Nijhof, et al. (2016)	29
3.8	Frequency analysis showing that the energy decays to zero at high frequencies . . . . .	30
3.9	Censored for confidentiality . . . . .	32
3.10	Soil layering in SILENCE . . . . .	32
3.11	Cumulative energy per cross-section . . . . .	34
3.12	Frequency spectrum compared with measurements at 750m . . . . .	35
3.13	Evolution of the noise 1/3 octave band SEL spectrum . . . . .	35
3.14	Evolution of the pressure in time and space . . . . .	36
3.15	Comparison of simulation vs. measurement SEL and $L_{p,pk}$ . Note that the internationally standard symbol for peak pressure ( $L_{p,pk}$ ) is denoted as $L_{peak}$ in the figure. . . . .	37
3.16	Normalized energy flux along the z-coordinate for various distances from the pile's surface . . . . .	38
3.17	Total energy that radiates back in the water column . . . . .	39
3.18	Frequency spectra 0.1m from the seabed . . . . .	39

3.19	Effect of the force amplitude on the energy radiation into the water column . . . . .	39
4.1	SEL Octave band spectra from the measurements, showing a baseline measurement without noise mitigation next to three different noise mitigation set-ups (Elzinga et al., 2019) . . . . .	42
4.2	Schematic representations of noise paths, compared to the bubble curtain and receiver location . . . . .	43
4.3	Coefficient Matrices. Red = 100% Transmission, Blue = 0% Transmission . . . . .	45
4.4	Description from the model (Bohne, Griefmann, and Raimund Rolfes, 2019) . . . . .	45
4.5	Comparison of the centerline velocity between simulation and original work (Bohne, Griefmann, and Raimund Rolfes, 2019) and measurements (Kobus, 1968) . . . . .	48
4.6	Schematic representations of Bubble curtain configurations, 1. Full block, 2. Partial block, 3. Artificial BBC . . . . .	49
4.7	Comparison between the SEL and $L_{p,pk}$ of the measurement data and the simulation with the bubble curtain. Note that the internationally standard symbol for peak pressure ( $L_{p,pk}$ ) is denoted as $L_{peak}$ in the figure. . . . .	50
4.8	Comparison of noise reduction in one-third octave bands . . . . .	50
5.1	$\Delta SEL$ and $\Delta L_{p,pk}$ for a bubble curtain placed at different ranges from the piles surface. . . . .	52
5.2	Rough approximation of the maximum horizontal distance over which the upward moving Mach cone can penetrate the water column. . . . .	53
5.3	Total energy that radiates back in the water column for the free field case . . . . .	53
6.1	Recommended approach for use of the effective source reduction . . . . .	58
A.2	Censored for confidentiality . . . . .	63
A.3	Censored for confidentiality . . . . .	63
B.4	Full block . . . . .	64
B.5	Partial block . . . . .	64
B.6	BBC model . . . . .	64

# List of Tables

1.1	Legislation on sound pressure level for offshore construction works in Germany, Belgium and The Netherlands . . . . .	2
2.1	Different impedances in the aquatic environment (Jensen et al., 2011; Hou et al., 2018) . . . . .	6
3.1	Variables for forcing function . . . . .	29
3.2	Stepsize, maximum and amount of the time and frequency vectors . .	30
3.3	Input parameters monopile . . . . .	31
3.4	Input parameters soil . . . . .	33
4.1	Unknown parameters (Bohne, Griebmann, and Raimund Rolfes, 2019)	48
5.1	Difference between minimum and maximum noise reduction for different cases . . . . .	52
6.1	Minimum radius per case and reduction potential . . . . .	56



# List of Abbreviations

<b>ADD</b> Acoustic Deterrent Device .....	2
<b>BBC</b> Big Bubble Curtain .....	2, 3, 13, 28, 42, 48, 49, 56
<b>BEM</b> Boundary Element Method .....	26, 27
<b>CPT</b> Cone Penetration Test .....	3, 31–33
<b>DBBC</b> Double Big Bubble Curtain .....	12, 42
<b>FE</b> Finite Elements .....	14, 58
<b>HSD</b> Hydro Sound Damper .....	13, 57
<b>NMS</b> Noise Mitigation System .....	1
<b>OWF</b> Offshore Wind Farm .....	1, 3, 9, 41, 50, 55, 56
<b>OWTG</b> Offshore Wind Turbine Generator .....	1, 27
<b>PDF</b> Probability Density Function .....	45, 46
<b>PE</b> Parabolic wave equation .....	14
<b>SBC</b> Small Bubble Curtain .....	13
<b>WI</b> Wavenumber integration .....	14



# Chapter 1

## Introduction

Offshore wind farms are becoming more important with the growing demand for the new renewable energy (Ramirez et al., 2020). To raise the capacity of the Offshore Wind Farms (OWF), Offshore Wind Turbine Generators (OWTG) are increasing in size (Ramirez et al., 2020; Seidel, 2014). To support larger turbines in the future, foundations must be able to support greater load, resulting in structures of greater physical stature.

The choice of foundation type depends on various parameters such as water depth, soil conditions, and wind farm size (Thomsen, 2014b). Ramirez et al. (2020) show that the most popular foundation concept is the monopile with 4,258 units installed (81% of all installed offshore wind turbine foundation types) up to date. This is because the monopile is fairly easy to install in water depths below 40 meters (Thomsen, 2014b). The most common method to install a monopile is impact piling (Thomsen, 2014a; Matuschek and Betke, 2009). The hammer strikes the monopile into the soil with hammer loads varying between 200-400 tonnes (Thomsen, 2014a). The noise intensity that is released from the blow of the hammer can easily exceed peak pressures of more than 200 dB re 1  $\mu Pa$  (Elzinga et al., 2019), which brings a serious risk of harming the aquatic environment. For example, the eardrum of a harbour porpoise can burst under the excitation of the impulsive sound load above 160 dB (Thomsen, 2014a). Marine mammals can easily suffer from permanent injury when they are in the vicinity of the pile during piling. But even when mammals are at a far distance from the site, the high-level noise still can influence their senses which can have an effect on their foraging behaviour (Bellmann, 2019).

It is legally required in the offshore industry to protect the environment when installing offshore wind farms. Consequently, governments adopt strict regulations when issuing permits. Companies must prove that the construction, maintenance and decommissioning will not cause severe environmental impact. Table 1.1 shows typical legislation that countries require to grant permits for offshore construction. Violation of this legislation could lead to a halt in offshore construction with severe delays as a consequence.

As mentioned before, piling noise can easily exceed peak pressure levels of 200 dB re 1  $\mu Pa$  (Elzinga et al., 2019). Hence, offshore companies employ noise mitigation systems (NMS) to attenuate their noise emissions. The NMS are deployed around the monopile. The noise that is produced by piling is reflected and transmitted by the NMS, the working principles differ per NMS. Several noise mitigation measures have been developed, the most commonly deployed are presented by Bellmann (2018)

Country	Indicator	Limit	Additional measures
Netherlands (Rijkswaterstaat, 2016)	SEL <sub>1</sub>	159-172 dB re 1 $\mu\text{Pa}^2$ at 750m	Acoustic Deterrent Device (ADD)
Germany (Müller and Zerbs, 2011)	SEL <sub>05</sub> , $L_{p,pk}$	160 dB re 1 $\mu\text{Pa}^2$ , 190 dB re 1 $\mu\text{Pa}$ at 750m	Max. piling time 3 hours
Belgium (Rumes et al., 2018)	$L_{p,pk}$	185 dB re 1 $\mu\text{Pa}$ at 750m	ADD

Table 1.1: Legislation on sound pressure level for offshore construction works in Germany, Belgium and The Netherlands

which can be found in chapter 2. Of all these different types, the Big Bubble Curtain (BBC) is used most often by the industry because of its simplicity in application and its efficiency in noise reduction (Tsouvalas and Metrikine, 2016). Studies have shown that BBC's do attenuate noise emissions to some extent (Bellmann, 2019; Lucke et al., 2011). Tsouvalas and Metrikine (2016) investigated the influence of the air volume, the thickness and the position of the air bubble curtain on the noise reduction level. However, effective radius of a BBC has not been studied yet. This research aims to fill this gap by looking at the criteria that determine how to position a BBC efficiently in terms of noise reduction.

## 1.1 Scope

In order to optimize a BBC efficiently for noise reduction, it requires a solid physical understanding of the underwater acoustic environment and the parameters that can influence the efficiency of the BBC system. Primarily, a literature study is conducted to gain an understanding in the parameters that play a role in underwater noise. In addition, the methodology of the model used in this study is presented. The model that is used in this research, from now referred to as SILENCE, is developed by Tsouvalas (2015) and Peng, Tsouvalas, and Metrikine (2019). In order to prove the validity of SILENCE, a validation study is performed beforehand. In this validation, SILENCE is compared to unmitigated acoustic measurement data obtained from the █████ offshore wind farm (Van Oord, 2018). After validation, a bubble curtain model is proposed to simulate the effect of the bubble curtain. The result of this study is validated against the mitigated measurement data from █████. The purpose of this study is to answer the following research questions:

*”What are the criteria for determining the optimal noise reduction position of the bubble curtain?”*

To answer this question the following sub questions have been defined:

- How accurate can SILENCE predict the sound exposure level (SEL) and peak pressure level ( $L_{p,pk}$ ) when compared to measured noise data in the case in which no noise mitigation is used?

- How Can a BBC be implemented in the SILENCE software including an elastic seabed description?
- What is the optimum distance in which a BBC needs to be placed in order to maximize the noise reduction potential?

### 1.1.1 Approach

To answer the previous questions the following approach is taken. First, a literature study is performed to discuss the topics of acoustics, specifically related to offshore pile driving. This includes learning about the source mechanisms of underwater noise, computational modelling of underwater noise and learning about the basic quantities in this field. In order to get introduced to the SILENCE software, a basic case study was analysed which additionally served the purpose of validation of the noise predictions with measured noise data collected in an offshore campaign. The validation is achieved by comparing numerical results to real-time measurement data, obtained at the █████ OWF (Van Oord, 2018). Note that the validation case is based on a free-field noise prediction without the inclusion of the BBC.

After the validation study, a bubble curtain is implemented. The bubble curtain implementation is achieved by means of introducing a frequency- and depth-dependent source strength reduction mechanism at the position of the BBC, i.e. the latter mechanism is defined by means of a transmission loss (TL) formula.. The damping characteristics of the bubble curtain are based on existing research. This scenario is also validated against measurements including the BBC. After validation a parametric study with the bubble curtain is performed. With the results of this parametric study, conclusions can be drawn related to the aforementioned questions and a recommendations is given.

### Limitations

Prior to the start of this research the following limitations are identified. The data that is provided by Van Oord contains measurements at the legally required 750m, plus extra measurements at 1500m and 5000m. The data contains input energies, sound exposure levels and peak pressure levels<sup>1</sup> which were taken at heights 2m and 10m from the seabed. However, a distinction between these depth levels is not made within the data-set. Nevertheless, Bellmann (2019) stated that there is hardly any difference observed between these depth levels. It means the validation is limited to the aforementioned levels meaning that simulation values in the soil or at other locations in the water column cannot be compared. Therefore it is assumed that if the SILENCE model complies with the data, the simulation at different levels is valid as well.

The CPT-data lacks dynamic tests. Therefore, wave speeds in the soil are estimated based on empirical formulas and literature.

In addition to the data-set, the simulation software has a limitation that could be identified in advance. In SILENCE, the seafloor is assumed to be flat. In reality, sand crests or troughs are located in the █████ field which may alter or even partially block noise paths (Jensen et al., 2011). This is handled by looking at the

---

<sup>1</sup>For a description of these quantities, the reader is referred to chapter 2

■■■■■ bathymetry where the measurements were situated. If there are locations where the bathymetry is flat than those locations are used for the validation studies. Another limitation of SILENCE, is the input force. This input force is approximated by a forcing function. This can bring an uncertainty in the model when it comes to predicting noise. In this research this can be handled by modifying the force by trial and error. It can generally be proven though that small modification in the time signature of the force will have minimum effect in the predicted SEL and  $L_{p,pk}$  for the pile dimensions considered here. What is of paramount importance is to be able to capture the correct amplitude of the force and the duration of the main impulse exerted by the impact hammer including the energy level of the hammer blow.

## 1.2 Thesis outline

Chapter 2 presents the literature study regarding this topic. Chapter 3, gives a synopsis on how the SILENCE model works and the validation study is also explained. After validation, the implementation of the bubble curtain is explained together with the validation of the effective source reduction method in chapter 4. The results of the parametric study are presented in chapter 5 of which conclusions are drawn and discussed in chapter 6.

# Chapter 2

## Theoretical background

This chapter presents the literature study related to the topic of this thesis. This chapter consists of the following: First of all, the fundamental acoustic quantities are studied. The focus in this chapter lies on the description of sound and the use of the decibel scale. Next, the physical aspects of sound are examined, together with the modeling of the sound propagation. After a basic knowledge of acoustics is discussed, underwater noise due to piledriving is examined by focusing on the generation of noise and the physical aspects that are of importance. Finally, an overview of the methodology for modeling underwater noise generated by offshore pile driving and noise reduction by air bubble curtain system is presented.

### 2.1 Acoustic fundamentals

Sound is usually generated by a source which could be any vibrating object. It causes pressure fluctuations in the ambient pressure which are detected by hydrophones or marine life. These pressure fluctuations radiate in all directions. Sound propagates at different speeds in diverse media. This is due to the contrast in density and the speed of sound through a medium. In the case of ocean acoustics, density and speed of sound are functions of salinity, temperature and static pressure, in which the latter is a function of depth (Jensen et al., 2011). An empirical approximation of the speed of sound in water ( $c_w$ ) is shown in equation 2.1.

$$c_w = 1449.2 + 4.6T_w - 0.055T_w^2 + 0.0029T_w^3 + (1.34 - 0.01T_w)(S - 35) + 0.016z \quad (2.1)$$

### 2.1.1 Acoustic quantities

#### Acoustic impedance

The relation between density ( $\rho$ ) and speed of sound ( $c$ ) is called acoustic impedance ( $Z$ ) (2.2). It represents the resistance that a material provides to an acoustic signal (Lefebvre, 1999). When sound travels through different media, the variation in impedance may deflect or even reflect the sound path. Table 2.1 shows several impedance levels that are related to the aquatic environment. A large difference in impedance between two media (such as water and soil) is often referred to as an impedance gap.

$$Z = \rho c \quad (2.2)$$

Type	Z [kg/(m <sup>2</sup> s)]
Seawater	$1.5 \cdot 10^6$
Silty sand	$3.2 \cdot 10^6$
Sandy silt	$2.7 \cdot 10^6$
Sand silt clay	$2.7 \cdot 10^6$
Silt	$2.6 \cdot 10^6$
Clayey silt	$2.4 \cdot 10^6$

Table 2.1: Different impedances in the aquatic environment (Jensen et al., 2011; Hou et al., 2018)

#### Pressure

Acoustic pressure is defined hereafter as the local variation in pressure in a certain medium additional to the static pressure (Lefebvre, 1999). Figure 2.1 shows a recording of such a pressure variation ( $p(t)$ ) in time ( $t$ ). The effective pressure of a recording is expressed as the root mean square value of the pressure ( $p_{rms}$ )(equation 2.3).

$$p_{rms} = \sqrt{\frac{1}{T_0} \int_{t_0}^{t_1} p(t)^2 dt} \quad (2.3)$$

Pressure fluctuations exist over a large dynamic range. This is why sound is usually expressed in sound pressure level (SPL). This is the ratio between  $p_{rms}$  and a reference pressure  $p_0$  of 1  $\mu$ Pa on a logarithmic scale (equation 2.4).

$$\text{SPL} = 20 \log \left( \frac{p_{rms}}{p_0} \right) \text{ dB re } 1 \mu\text{Pa} \quad (2.4)$$

A common quantity in ocean acoustics is the peak pressure level ( $L_{p,pk}$ ). This is for example used in Belgian legislation to mark the limit pressure level during offshore piling (Table 1.1). The peak pressure is the ratio between the maximum pressure and reference pressure  $p_0$ . Figure 2.1 shows a visual representation of the peak pressure<sup>1</sup>. The peak pressure level is commonly expressed in Decibels as shown

<sup>1</sup>Sometimes acousticians prefer the peak-to-peak pressure as can be seen in figure 2.1. This quantity is not used in this research.

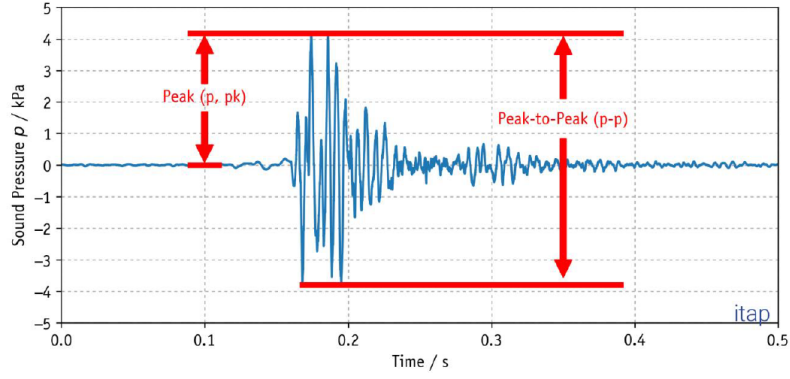


Figure 2.1: An example of a pressure recording in time (Bellmann, 2019)

in expression 2.5.

$$L_{p,pk} = 20 \log \left( \frac{\max |p(t)|}{p_0} \right) \text{ dB re } 1 \mu\text{Pa} \quad (2.5)$$

### Intensity

Intensity<sup>2</sup> is the average rate of flow of energy through a unit area that is normal to the direction of propagation (Jensen et al., 2011). It relates to average pressure and impedance (equation 2.6) and is expressed in  $\text{W}/\text{m}^2$ .

$$I = \frac{p_{rms}^2}{Z} \quad (2.6)$$

### Sound exposure

Exposure ( $E$ ) is the sound pressure squared, averaged over a certain period of time. It is calculated according to equation 2.7 and expressed in  $\text{Pa}^2 \cdot \text{s}$ .

$$E = \int_{t_1}^{t_2} p(t)^2 dt \quad (2.7)$$

Like other quantities in acoustics, exposure is also commonly expressed in the logarithmic scale in the form of sound exposure level (SEL). This is the exposure level compared to the reference exposure level  $E_0$ .

$$\text{SEL} = 10 \log \left( \frac{E}{E_0} \right) = 10 \log \left( \int_{t_1}^{t_2} \frac{p^2(t)}{p_0^2} dt \right) \text{ dB re } 1 \mu\text{Pa}^2\text{s} \quad (2.8)$$

Like  $L_{p,pk}$ , SEL is also a measure which is used in legislation to quantify limits during offshore piling (table 1.1).

<sup>2</sup>Note that intensity ratios can also be expressed on the logarithmic scale in the form of SIL (Sound intensity level). Since this quantity is not commonly used in this research, it will not be addressed for the sake of brevity.

### 2.1.2 The decibel scale

As can be seen from the above mentioned quantities, the decibel scale is commonly used in acoustics. Counter-intuitively, the decibel is **not** a unit. It is actually a ratio between values, such as power, intensity or exposure, expressed on a logarithmic scale (Chapman and Ellis, 1998). Due to the large dynamic range of sound, it is easier to work with decibels than with absolute pressure values. However, it is important to note that what seems a small change on the decibel scale, is actually a large change in non-logarithmic values. For example, the logarithmic scale means that a change of pressure by a factor 10 corresponds to a 10 dB change. But a 30 dB change is already 1000 times larger. This is mentioned to emphasize the importance of the decibel scale being used in the right manner.

### 2.1.3 The Helmholtz equation

Acoustic modelling is based on wave propagation theory (Jensen et al., 2011). It describes how waves propagate in space and time. The acoustic wave equation stems from linearized equations of mass conservation (2.9), momentum conservation (2.10) and the adiabatic equation of state (2.11).

$$\frac{\partial \rho}{\partial t} = -\nabla \cdot (\rho \mathbf{v}) \quad (2.9)$$

$$\frac{\partial \mathbf{v}}{\partial t} = -\frac{1}{\rho} \nabla p(\rho) \quad (2.10)$$

$$\frac{\partial p}{\partial t} = c^2 \left( \frac{\partial \rho}{\partial t} + \mathbf{v} \cdot \nabla \rho_0 \right) \quad (2.11)$$

By combining equation 2.9, 2.10 and 2.11, the wave equation can be described. This can be expressed for pressure ( $p$ ), velocity ( $v$ ), velocity potential ( $\phi$ ) and displacement potential ( $\psi$ ) (Jensen et al., 2011). The wave equation for the displacement potential is presented in equation 2.12.

$$\nabla^2 \psi - \frac{1}{c^2} \frac{\partial^2 \psi}{\partial t^2} = f_e(\mathbf{r}, t) \quad (2.12)$$

By applying the Fourier transform pair (2.13) to (2.12), one obtains the Helmholtz equation (3.31), which is basically the wave equation for displacement potential in frequency domain.

$$\tilde{f}(\omega) = \int_{-\infty}^{\infty} f(t) e^{-i\omega t} dt, \quad f(t) = \frac{1}{2\pi} \int_{-\infty}^{\infty} \tilde{f}(\omega) e^{i\omega t} d\omega \quad (2.13)$$

$$[\nabla^2 + k(\mathbf{r})^2] \psi(\mathbf{r}, \omega) = f(\mathbf{r}, \omega) \quad (2.14)$$

Here,  $\nabla^2$  is the well known Laplace operator that depends on the used coordinate system. The wavenumber  $k$  is described in equation 2.15. The vector  $\mathbf{r}$  describes the coordinates in space.  $\omega$  describes the frequency.

$$k(\mathbf{r}) = \frac{\omega}{c(\mathbf{r})} \quad (2.15)$$

## 2.2 The sources of noise

In this section, the sources of noise are described. The hammer blow induces a pile response which induces waves in both the water and soil media. This section is set up in such a way that the contributions to underwater noise are treated individually in the following subsections. Following the energy path in Figure 2.2, the hammer (a) is described in 2.2.1. Next, a compressional wave is induced which creates a Mach cone in the fluid (b). This is explained in 2.2.2. When the soil is induced by the pile response, two types of waves are occur: surface waves (c) and body waves (d). They are described in 2.2.3 and 2.2.4

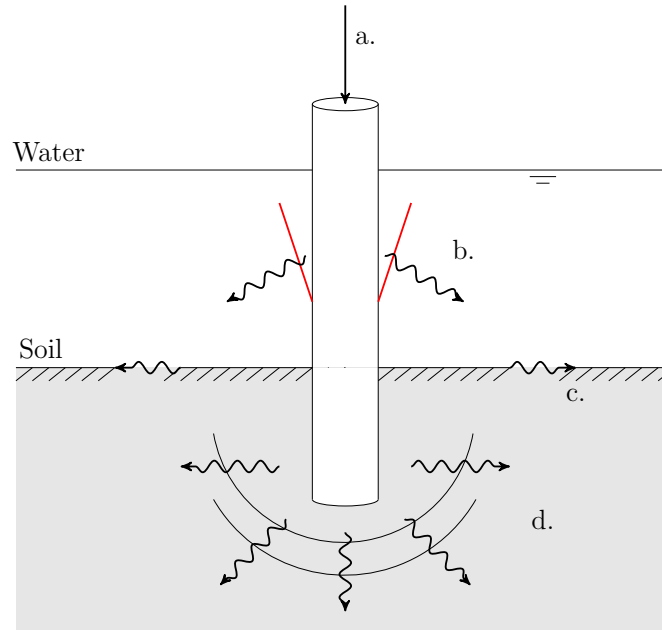


Figure 2.2: Processes of noise during offshore piling

### 2.2.1 Hammer impact

When installing a monopile, the prime source of energy comes from the hydraulic hammer. During the construction of the ██████ offshore wind farm (OWF), the Menck MHU-3500S was used for piling. Therefore, the data from this hammer is used in this study. The MHU-3500S can drive 30 blows every minute with an energy input between 350 and 3500 kJ (Menck GmbH, 2016). One ram provides a weight of 175 tonne on the pile (Menck GmbH, 2016).

### 2.2.2 Pile response

The blow of the hammer induces a force and a particle velocity that causes a compression wave in the structure (Reinhall and Dahl, 2011; Kuhn et al., 2014). This wave propagates in downward axial direction with a speed  $c_p$ <sup>3</sup> which is dependant

<sup>3</sup>Note that this is an approximation for a 1D bar. In reality the wave speeds are dispersive in piles of very large diameter partly embedded in the soil. This makes the wave speed frequency dependent in reality. However, the influence is negligible since the pile is surrounded with media with much lower wavespeeds.

on the Young's modulus  $E_s$  and density  $\rho_s$  of the steel (2.16). The compression wave causes a local increase of the pile's radius due to the Poisson's effect (Reinhall and Dahl, 2011; Kuhn et al., 2014).

$$c_p = \sqrt{\frac{E_s}{\rho_s}} \quad (2.16)$$

At the pile tip, the compression wave is reflected into a tension wave which propagates upwards due to the impedance mismatch between the soil and steel (Reinhall and Dahl, 2011). It causes a local decrease in the pile's radius. Figure 2.3 shows a schematic representation of the compression and tension wave traveling in axial direction.

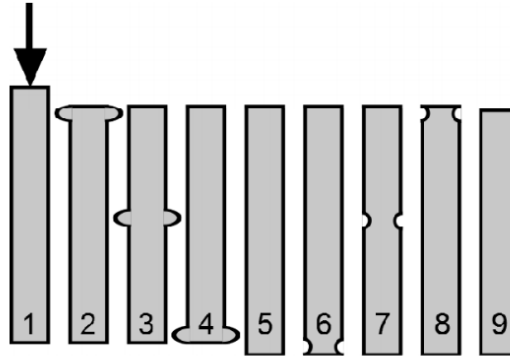


Figure 2.3: Compression strain wave in the pile (Kuhn et al., 2014)

Both the increasing and decreasing deformations cause pressure fluctuations in the surrounding media. The deformations travel along the pile with a wave speed ( $c_p \approx 5000$  m/s) larger than the wave speed in water and soil. This causes the acoustic pressure field to take a conical form, commonly referred to as a Mach cone (Reinhall and Dahl, 2011). The angle of the Mach cone follows straightforward from equation 2.17. Where the angle in water ( $\varphi_w$ ) and soil ( $\varphi_s$ ) are approximately  $17.2^\circ$  and  $18.6^\circ$  respectively (Reinhall and Dahl, 2011).

$$\varphi = \sin^{-1} \left( \frac{c}{c_p} \right) \quad (2.17)$$

The reflected tension wave, also produces a Mach cone which moves in upward direction. In the sediment, the cone has an angle of  $\varphi_s$ . When the upward moving Mach cone penetrates the water,  $\varphi_s$  is refracted into an angle  $\varphi_{ws}$  ( $\approx 30^\circ$ ) following Snell's law (eq. 2.18) (Reinhall and Dahl, 2011; Jensen et al., 2011). This finally results in two upward moving wave fronts with an angle  $\varphi_w$  and  $\varphi_{ws}$ , where the former is produced by the up-moving wave front from the tension wave (Reinhall and Dahl, 2011). A schematic representation is shown in Figure 2.5.

$$\frac{\cos(\varphi)}{c} = \text{const} \quad (2.18)$$

It is important to note that the Mach wave, generated by the structural response of the pile, is the dominant source of underwater noise (Reinhall and Dahl, 2011; Tsouvalas, 2015).

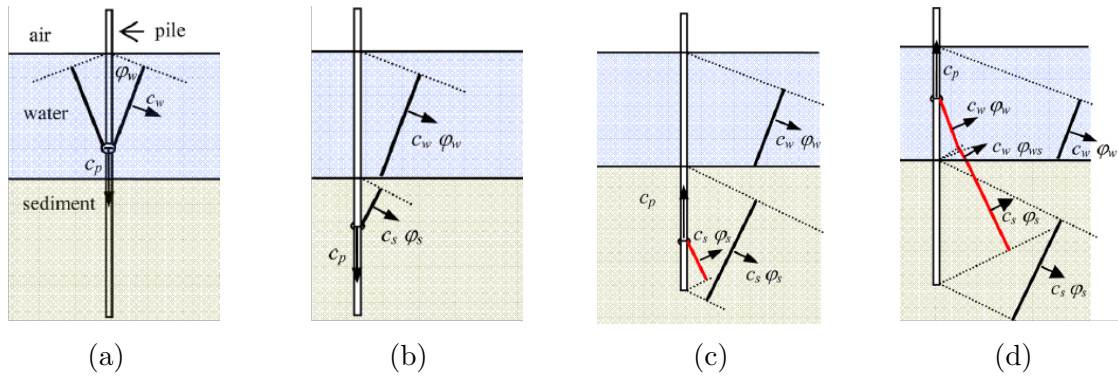


Figure 2.4: Chain of events of the Mach cone generation during a hammer blow, showing the different angles, wave speeds and direction of propagation. Figure (a) and (b) show the wave front going into the sediment. Note that the angle of the Mach cone changes. Figure (c) and (d) show the reflected waves traveling upward back into the watercolumn (Reinhall and Dahl, 2011).

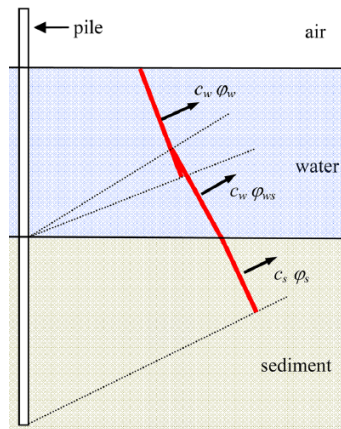


Figure 2.5: Resultant wave fronts after reflection in the pile (Reinhall and Dahl, 2011)

### 2.2.3 Surface waves

A surface wave is a wave that travels on the interface between two media (Meegan et al., 1999). An example of surface waves are ocean waves which travel on the interface between a liquid and a gas. There are three fundamental types of surface waves in isotropic media (Meegan et al., 1999): Rayleigh waves (solid-vacuum interface), Stoneley waves (solid-solid interface) and Scholte waves (solid-fluid interface) (Meegan et al., 1999). In the topic of underwater noise, surface waves exist at the soil-water interface. This can be identified as solid-fluid interface waves i.e. Scholte waves. Scholte waves are non-dispersive of nature, which means their phase velocity is independent of wavenumber. This means that all Scholte waves, of any wavenumber/frequency travel at the same phase velocity. This phase velocity of the Scholte wave does depend on the stiffness of the solid medium (Glorieux et al., 2001). The stiffer the soil, the higher the phase velocity (Glorieux et al., 2001). Because Scholte waves travel on an interface, they travel in cylindrical direction. Therefore, they decay less rapidly with distance compared to spherically traveling body waves (Meegan et al., 1999).

### 2.2.4 Seismic waves

Body waves travel through the inside of the seabed (Yilmaz and Miller, 2015). Figure 2.6 shows the difference the two types of body waves. The compressional waves (P-waves) are a result of the Mach pressure wave (Tsouvalas, 2015) and of the downward movement at the pile tip. The shear waves (S-waves) are a result of the downward movement of the pile, where the friction between the pile wall and the soil cause an elastic deformation in vertical direction. Shear waves can be characterized in vertical (SV-waves) and horizontal (SH-waves) polarized waves. The difference is whether the particle moves in vertical or horizontal direction. Tsouvalas (2015), showed that (almost) vertical polarized shear waves are more dominant compared to the compressional waves during offshore pile driving. The body waves radiate spherically, resulting in waves partially entering the water column and partially going deeper into the sediment.

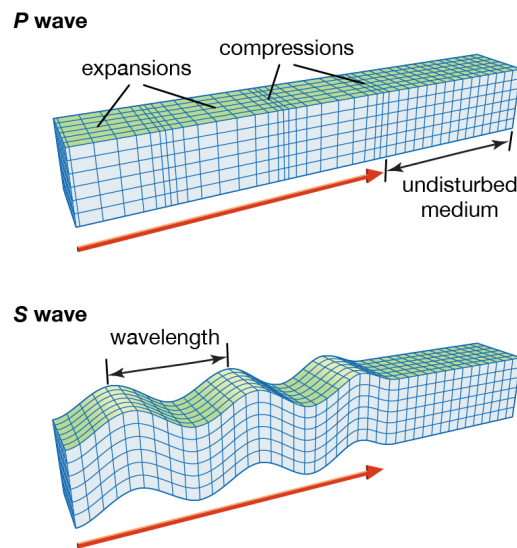


Figure 2.6: S-waves and P-waves (Britannica, 2020)

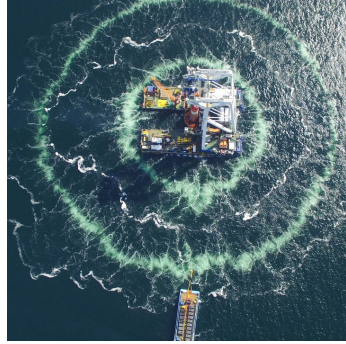
## 2.3 State of the art noise mitigation techniques

Several noise mitigation systems have been developed for the past years. Some are operational and some are still being tested. There are many more types available but the systems mentioned below are thoroughly tested under offshore conditions and are widely applied in the industry. For the description of these mitigation systems an overview by Bellmann (2018) is consulted.

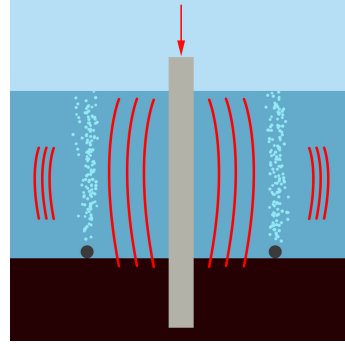
### 2.3.1 Single and Double Big Bubble curtains (BBC and DBBC)

A (double) bubble curtain (BBC or DBBC) is a hose lying on the seabed. Air is pumped into the hose which contains nozzles. This creates a curtain of bubbles. A bubble curtain has two working principles. First is the impedance mismatch between the water and the air-bubble mixture. Second is that the bubbles work as

resonators (Tsouvalas and Metrikine, 2016). The first impedance mismatch accounts for reflection. The resonating bubble accounts for the transfer of acoustic energy near the natural frequencies of the bubbles (Tsouvalas and Metrikine, 2016). Figure 2.7 shows how bubble curtains are used in practice. A downside of a BBC is that current affects the shape of the curtain.



(a) Bubble curtain in action (Van Oord, 2016)



(b) Schematic representation

Figure 2.7: The working principle of bubble curtains.

### 2.3.2 Small Bubble Curtain (SBC)

The SBC uses multiple nozzle hoses close to the pile. These hoses are aligned vertically between the seabed and the surface. The distance between the hoses is less than 0.5 m. This creates a full bubble medium around the pile which ensures that the pile is installed in a bubble/water medium.

### 2.3.3 Hydro Sound Damper (HSD)

The Hydro sound damper (HSD) has a net filled with foam elements. These elements have different sizes and are placed at different distances. The HSD system has a ballast ring at the bottom and a floater at the top. It is placed around the pile at a short distance ( $\approx 5-6$  m). Elements can be plastic foam or gas-filled balloons. It attenuates sound the same way as bubble curtains. However, this is a static structure and will therefore not be influenced by any current. Figure 2.8 shows a schematic representation of the HSD.

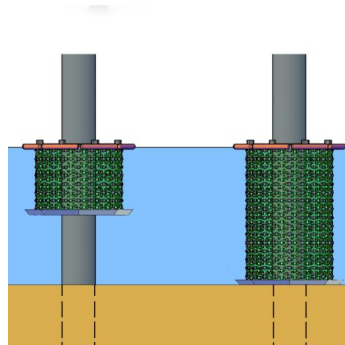


Figure 2.8: Schematic representation of HSD (Elmer and Savery, 2014)

### 2.3.4 Noise mitigation screen (IHC-NMS)

An IHC noise mitigation system (IHC-NMS) is a double walled steel tube which surrounds the pile. The space between the walls is filled with air. Additionally, air bubbles can be fed into the water column. Sound passes through two barriers. The noise will be reduced due to reflection.

### 2.3.5 Cofferdam

The cofferdam is a single walled steel tube. It seals off the area where the pile is installed. Using a seal ring, the water can be evacuated from the space between the pile and the cofferdam. Using a cofferdam, one can in basically install a pile in air. Noise is radiated to the cofferdam into the water. The impedance gap between air and water results in the noise being reflected and thus attenuated.

### 2.3.6 AdBm

The AdBm system is a novel system that does not work primarily because of an impedance gap. The AdBm system contains Helmholtz resonators to attenuate the sound due to pile driving (Froeze, 2019). The application of these resonators can be customized for any particular offshore project because specific frequencies can be targeted which produce the most damaging noise (Skopljak, 2019).

## 2.4 Noise prediction models

Noise prediction in offshore piledriving has been of interest to deal with uncertainties in environmental management and to reduce construction delays. Therefore, several models have been developed. Reinhall and Dahl (2011) were the first to develop a model to measure the noise levels as a result of pile driving. Their simulation was based on a Finite Element simulation (FE) combined with a parabolic wave equation (PE) in a shallow water waveguide with a vertical distribution of phased point sources, which magnitudes are determined by the FE model (Reinhall and Dahl, 2011).

With this model, they showed that the primary source of underwater noise comes from the compression in the pile and the radial displacement related to it, resulting in a Mach wave front traveling through its surrounding media (Reinhall and Dahl, 2011). This is also shown in figure 2.9. In this model the soil was modelled as an equivalent fluid, meaning that shear waves and Scholte waves were not accounted for.

Lippert and Lippert (2012) proposed a propagation model based on a wavenumber integration (WI) approach. They used this technique because a full FE model is computationally expensive for predicting noise at large distances and many frequencies. Therefore, a combination of an FE model together with a propagation model takes less computational effort. Lippert and Lippert (2012) validated their work based on the FE simulations by Reinhall and Dahl (2011) and found that this approach is in agreement with the FE simulations. This model also assumes two layers, of which the soil is modelled as an equivalent fluid, neglecting the shear and Scholte waves.

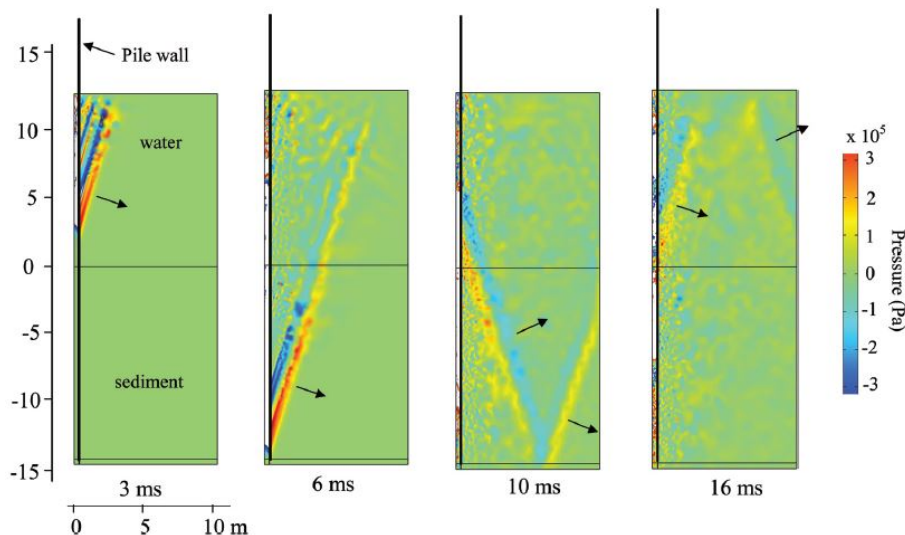


Figure 2.9: Mach wave radiation (Reinhall and Dahl, 2011)

Zampolli et al. (2013) studied this topic by means of a linear structural acoustic finite element model without making use of a propagation model. They found that this model can be used for understanding the acoustic radiation from the pile. They recommended that the coupling between the sediment and the pile, the forcing and the modelling of the source required further investigation.

Note that the models described above are based on Finite Element simulations which are an extension of the work of Reinhall and Dahl (2011).

Tsouvalas (2015) was the first to model the vibro-acoustic problem fully with a normal mode method. This is referred to as the SILENCE model. Here the pile was modelled with thin shells. Compared to previous models, the entire problem was solved by using normal modes and by coupling the pile, water and soil behaviour through boundary and interface conditions. The model was solved in frequency domain which makes this model computationally very efficient. The model has a rigid bottom assumption at the bottom of the lowest sediment layer. This makes the near field solution bounded to noise near the pile. Peng, Tsouvalas, and Metrikine (2019) extended this model with a far-field solution that overcomes this problem. Here, the solution in the near field model is extended over large distances. In previous studies, the SILENCE model was able to predict sound exposure levels and peak pressure within  $\pm 2$  dB.

## 2.5 Bubble curtain models

To predict the noise emitted from offshore piling, it is desired to have a model that also captures the effect of several mitigation systems (see section 2.3). When the noise and damping of it become more predictable, better forecasts can be made which results in better understanding, protection of wildlife and less delay during construction.

The basic principles of attenuation by a bubble curtain are the impedance mismatch and the transfer of acoustic energy near the natural frequency. The maximum transfer of energy between the bubble and an incident wave is at the natural frequency of the bubble. Hence, the strongest sound attenuation is close to the natural

frequency (Minnaert, 1933). Additionally, the impedance mismatch between the water and the bubble causes a reflection. Even though the principle of attenuation by a bubble is well known, the attenuation of noise by a bubble curtain under offshore conditions is still being investigated (Bohne, Griebmann, and Raimund Rolfes, 2019).

Göttsche (2013) developed a model to assess the noise reduction by a small bubble curtain. The bubble distribution was determined by CFD analysis, with this analysis the volume fraction was solved. The bubble size was approximated by a normal distribution with an average of 10mm. The near field noise emissions were modelled using a finite element analysis. The source spectrum was then reduced by a transmission coefficient. This method neglected the physical characteristics such as reflection and propagation through the bubble curtain. The model was in good agreement with measurements.

Tsouvalas and Metrikine (2016) expanded the SILENCE model with a bubble curtain by adding a vertical homogeneous domain in the fluid layer. The bubble curtain was described with frequency dependent, complex-valued compressibility which gave the ability to approximate realistic wavenumbers related to piledriving. They showed that, for large diameter piles and a small bubble size, the most attenuation comes from the impedance mismatch between the water and the bubbles. However, when the acoustic energy is concentrated at frequencies larger than the natural frequency of the bubble, the sound absorption becomes critical. Thus, the bubble thickness is a critical parameter.

Lippert, Huisman, et al. (2017) applied a double big bubble curtain by implementing two non-reflecting impedance boundary conditions in their model. These boundary conditions mimic a perfect absorbing bubble curtain which absorbs the pressure waves in the water column.

Bohne, Griebmann, and Raimund Rolfes (2019) developed a modelling approach of a big bubble curtain in offshore conditions. They first calculated the local wavenumber distribution. Here, the bubble radii were approximated by a lognormal distribution based on measurements. With the local wavenumber computed, the transmission characteristics of a bubble curtain were determined. The approach allowed an appropriate estimate of the noise mitigation by a bubble curtain. Their advice is that this modelling approach is promising but it may be improved by modelling the environmental conditions with it, such as currents. This is of interest for future research. Since this model uses a non-uniform distribution of bubbles and an increasing width of the bubble curtain. The derivation of transmission coefficients in this work are based on the aforementioned model(Bohne, Griebmann, and Raimund Rolfes, 2019).

# Chapter 3

## Modeling underwater noise

This chapter discusses the modeling strategies used in this work. In this research, the SILENCE model is used. This is a semi-analytic model based on the normal mode method. Prior to working with SILENCE, the Normal mode method is investigated for clarification. This is explained with a simple problem in section 3.1. The modeling strategy, used in SILENCE, is discussed in sections 3.2 and 3.3. Finally, the strategy for validating the model is set out in section 3.4. In addition, the data-set that has been made available (Van Oord, 2018) to validate SILENCE is discussed.

### 3.1 Moving point source model

This subsection elaborates on the math behind the normal mode method by means of a relatively simple problem. First, the mathematical derivation is shown based on Jensen et al. (2011). This derivation explains the solution strategy for a point source in cylindrical geometry. This setup is chosen because it explains the basic concept of normal modes well. Additionally, a practical problem was solved based on the work of Jensen et al. (2011) and Lippert and Lippert (2012) where the point source is moved in time such that a Mach wave is generated. The goal of modeling this was to get familiar with the concept of the normal mode method prior working with a more complex model like SILENCE.

#### 3.1.1 Mathematical derivation

Here, the mathematical derivation of a point source in cylindrical geometry is presented based on Jensen et al. (2011). The Helmholtz equation for a point source in cylindrical geometry is defined in (3.1).

$$\frac{1}{r} \frac{\partial}{\partial r} \left( r \frac{\partial p}{\partial r} \right) + \rho(z) \frac{\partial}{\partial z} \left( \frac{1}{\rho(z)} \frac{\partial p}{\partial z} \right) + \frac{\omega^2}{c^2} p(r, z) = -\frac{\delta(r) \delta(z - z_s)}{2\pi r} \quad (3.1)$$

It can be solved using the separation of variables technique where a solution in the form of  $p(r, z) = \Phi(r)\Psi(z)$  is sought. Substituting  $p(r, z)$  in the the unforced equation and dividing by  $\Phi(r)\Psi(z)$  yields (3.2).

$$\frac{1}{\Phi(r)} \left[ \frac{1}{r} \frac{d}{dr} \left( r \frac{d\Phi}{dr} \right) \right] + \frac{1}{\Psi(z)} \left[ \rho(z) \frac{d}{dz} \left( \frac{1}{\rho(z)} \frac{d\Psi(z)}{dz} \right) + \frac{\omega^2}{c^2} \Psi(z) \right] = 0 \quad (3.2)$$

Equation 3.2 contains two equations of the separated variables  $r$  and  $z$ . The only way these equations can be satisfied is if they equal a constant, the separation constant  $k_{rm}^2$ . The modal equation (3.3) is obtained by equating the  $z$ -dependant part of (3.2) with  $k_{rm}^2$ .

$$\rho(z) \frac{d}{dz} \left[ \frac{1}{\rho(z)} \frac{d\Psi_m(z)}{dz} \right] + \left[ \frac{\omega^2}{c^2} - k_{rm}^2 \right] \Psi_m(z) = 0 \quad (3.3)$$

The boundary conditions that are imposed on this problem are the pressure release surface (3.4) and a rigid bottom (3.5).

$$\Psi(0) = 0 \quad (3.4)$$

$$\left. \frac{d\Psi}{dz} \right|_{z=D} = 0 \quad (3.5)$$

The modal equation is a Sturm-Liouville eigenvalue problem which has the following properties:

- The modal equation has an infinite number of solutions (modes).
- Each mode is a modeshape function  $\Psi_m(z)$  that contains a propagation constant  $k_{rm}$ .
- $\Psi_m(z)$  is an eigenfunction and  $k_{rm}^2$  an eigenvalue.
- The eigenvalues  $k_{rm}^2$  are all real.
- The modes are orthogonal (3.6), (3.7)

$$\int_0^D \frac{\Psi_m(z)\Psi_n(z)}{\rho(z)} dz = 0 \quad \text{for } m \neq n \quad (3.6)$$

$$\int_0^D \frac{\Psi_m^2(z)}{\rho(z)} dz = 1 \quad \text{for } m = m \quad (3.7)$$

All modes will form a complete set. This means that the solution to (3.1) can be expressed as a summation of modes (3.8) that converges to a total solution for the motion in the medium.

$$p(r, z) = \sum_{m=1}^{\infty} \Phi_m(r) \Psi_m(z) \quad (3.8)$$

Substituting this in (3.1) yields

$$\begin{aligned} \sum_{m=1}^{\infty} \left\{ \frac{1}{r} \frac{d}{dr} \left( \frac{d\Phi_m(r)}{dr} \right) \Psi_m(z) + \Phi_m(r) \left[ \rho(z) \frac{d}{dz} \left( \frac{1}{\rho(z)} \frac{d\Psi_m(z)}{dz} \right) + \frac{\omega^2}{c^2} \Psi_m(z) \right] \right\} \\ = - \frac{\delta(r)\delta(z - z_s)}{2\pi r} \end{aligned} \quad (3.9)$$

Note that the term in the square brackets equals  $k_{rm}^2$  (3.3). This yields (3.10).

$$\sum_{m=1}^{\infty} \left\{ \frac{1}{r} \frac{d}{dr} \left( \frac{d\Phi_m(r)}{dr} \right) \Psi_m(z) + k_{rm}^2 \Phi_m(r) \Psi_m(z) \right\} = -\frac{\delta(r)\delta(z-z_s)}{2\pi r} \quad (3.10)$$

By making use of the orthogonality property ((3.6), (3.7)), equation 3.10 is multiplied with  $\Psi_n(z)/\rho(z)$  and integrated over the depth. This yields equation 3.11.

$$\frac{1}{r} \frac{d}{dr} \left[ r \frac{d\Phi_n(r)}{dr} \right] + k_{rn}^2 \Phi_n(r) = -\frac{\delta(r)\Phi_n(z_s)}{2\pi r \rho(z_s)} \quad (3.11)$$

The solution to (3.11) is a standard solution in terms of a Hankel function.

$$\Phi_n(r) = \frac{i}{4\rho(z_s)} \Psi_n(z_s) H_0^{(1,2)}(k_{rn}r) \quad (3.12)$$

Substituting (3.12) into (3.8) yields the solution to the pressure field in frequency domain.

$$p(r, z, \omega) = \frac{i}{4\rho(z_s)} \sum_{m=1}^{\infty} \Psi_m(z_s) \Psi_m(z) H_0^{(1,2)}(k_{rm}r) \quad (3.13)$$

This solution is used in the following problem, the isovelocity problem (Jensen et al., 2011).

### 3.1.2 Isovelocity problem

This problem is an extended version of the isovelocity problem (figure 3.1) by moving the point source down the z-axis (Lippert and Lippert, 2012). By moving the point source in time, a Mach cone is simulated (Lippert and Lippert, 2012).

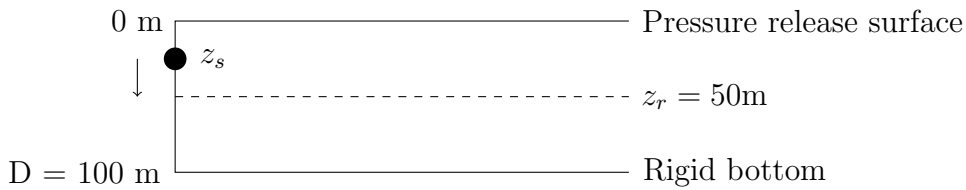


Figure 3.1: The isovelocity problem (Jensen et al., 2011)

In this problem, it is assumed that the density and wavespeed are constant in the entire domain. The problem to solve is basically equation (3.3), (3.4) and (3.5). The general solution to the problem is shown in (3.14).

$$\Psi_m(z) = A \sin(k_z z) + B \cos(k_z z) \quad (3.14)$$

The vertical wavenumber  $k_z$  is defined by

$$k_z = \sqrt{\frac{\omega^2}{c^2} - k_r^2} \quad (3.15)$$

The pressure release surface boundary condition (3.4), states that  $B = 0$  whereas the rigid bottom boundary condition states:

$$Ak_z \cos(k_z D) = 0 \quad (3.16)$$

This means either  $A = 0$  (trivial solution) or

$$k_{zm} = \left(m - \frac{1}{2}\right) \frac{\pi}{D} \quad m = 1, 2, \dots \quad (3.17)$$

With equation (3.15),  $k_{rm}$  can be determined.

$$k_{rm} = \sqrt{\frac{\omega^2}{c^2} - \left[\left(m - \frac{1}{2}\right) \frac{\pi}{D}\right]^2}, \quad m = 1, 2, \dots \quad (3.18)$$

$A$  is determined on the basis of the orthogonality property (3.7) yielding

$$A = \sqrt{\frac{2\rho}{D}} \quad (3.19)$$

The eigenfunction thus becomes

$$\Psi_m(z) = \sqrt{\frac{2\rho}{D}} \sin(k_{zm}z) \quad (3.20)$$

This is substituted in equation (3.13) finally yielding the pressure function in frequency domain for a certain  $z_s$ .

$$p(r, z, \omega) = \frac{i}{2D} \sum_{m=1}^{\infty} \sin(k_{zm}z_s) \sin(k_{zm}z) H_0^{(1)}(k_{rm}r) \quad (3.21)$$

The time domain solution can be obtained by applying the inverse fourier transform (3.22) to (3.21).

$$p(r, z, t) = \frac{1}{2\pi} \int_{-\infty}^{+\infty} p(r, z, \omega) e^{-i\omega t} d\omega \quad (3.22)$$

This is calculated numerically with (3.23). Which computes the pressure field shown in figure 3.3.

$$\frac{1}{2\pi} \sum_{m=1}^M \{p(r, z, \omega) e^{-i\omega t_m} \Delta\omega\} \quad m = 1, 2, \dots, M \quad (3.23)$$

The extension of this problem is based on the work of Lippert and Lippert (2012). They model a Mach cone by moving a point source in time. The movement of the point source is modelled by introducing a phase  $\epsilon$  in the Fourier transform. The Fourier transform is calculated for each phase shift and then superimposed to each other.

$$\frac{1}{2\pi} \sum_{n=1}^N \sum_{m=1}^M \{p(r, z, z_{s,n}, \omega) e^{-i\omega(t_m - \epsilon_n)} \Delta\omega\} \quad m = 1, 2, \dots, M \quad n = 1, 2, \dots, N \quad (3.24)$$

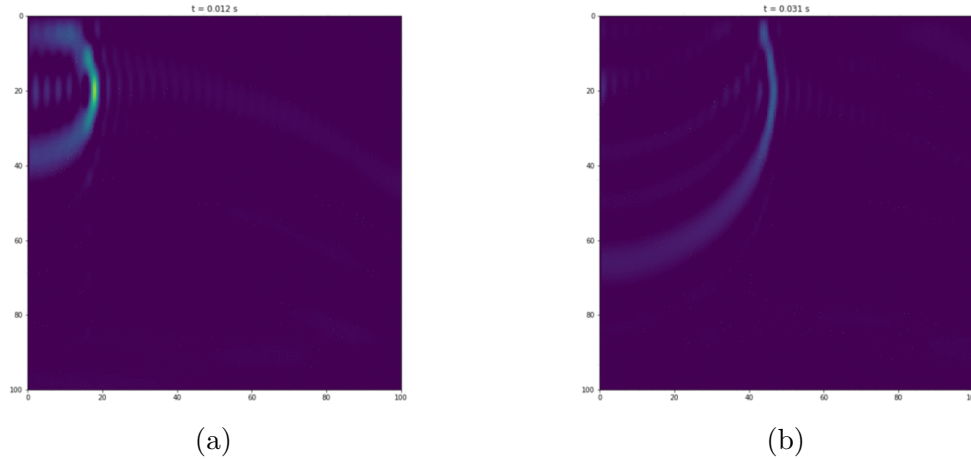


Figure 3.2: Pressure field time domain solution to the isovelocity problem

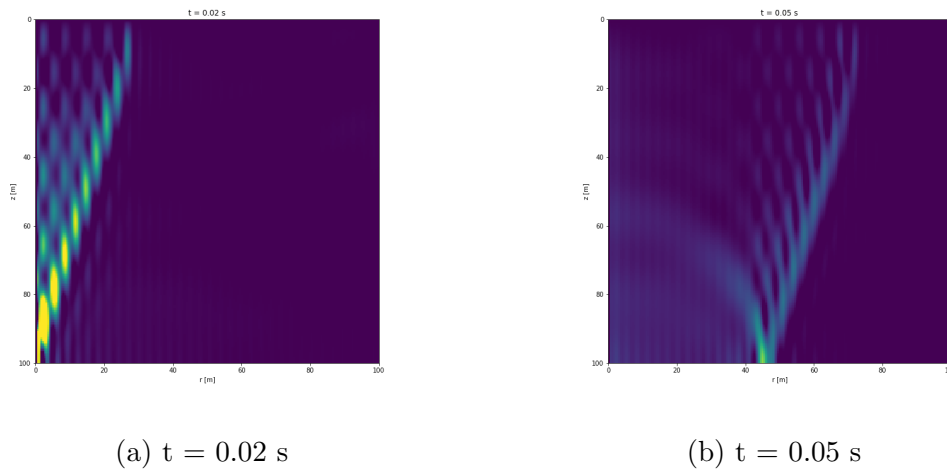


Figure 3.3: Mach cone by moving a point source in time

This results in a pressure field where a pulse is generated after every phase shift. Every phase shift is calculated by  $\Delta z/c_s$ , where  $c_s$  is approximately 5000 m/s. The Mach cone propagates through water with a wave speed of  $c_w = 1500\text{m/s}$ . The angle of the Mach cone is approximately  $17^\circ$ , which corresponds to the given angle in subsection 2.2.2.

When the wave hits the bottom, a reflected wave is observed due to the rigid boundary condition. This reflected wave is not realistic. The results from a simulation may become distorted by the reflected wave after some time. Such events, are the consequence of modeling assumptions. It is important to note that these assumptions also occur in advanced models and should therefore be considered carefully.

## 3.2 SILENCE Near field model

In this section, the Near-Field model of the SILENCE model is described. First, the configuration and assumptions are discussed. Then the governing equations are presented. The information from the following subsections comes from , Tsouvalas

(2015) and Tsouvalas (2020). A detailed description of solution strategy of the model is beyond the scope of this work. Therefore, the reader is advised to consult Tsouvalas (2015) and Tsouvalas (2020) for detailed derivations.

The SILENCE Near-Field model contains a pile, a fluid and a soil domain as shown in figure 3.4. The sub-domains are described in the following subsections.

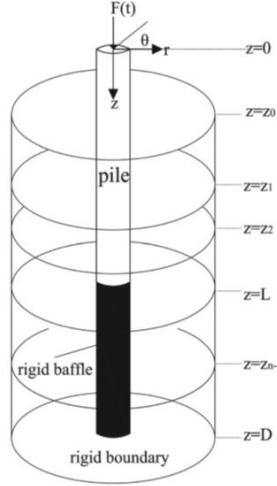


Figure 3.4: SILENCE Near-Field model geometry (Tsouvalas, 2015)

### 3.2.1 Pile

The pile is modelled in the domain  $0 \leq z \leq L$  and  $0 \leq r \leq R$ . To account for shear deformation and rotational inertia, a thin shell theory as described by Kaplunov, Kossovitch, and Nolde (1998). The parameters that describe the nature of the shell are  $E$ ,  $\rho$ ,  $\nu$ ,  $R$ ,  $t$  and  $L$  which are complex E-modulus, density, Poisson's ratio, radius, thickness and length respectively.

The governing equations for the shell vibrations are described in the following equation:

$$\mathbf{L}\mathbf{u}_p + \mathbf{I}\ddot{\mathbf{u}}_p = (H(z - z_1) - H(z - L))\mathbf{t}_s - (H(z - z_0) - H(z - z_1))\mathbf{p}_f + \mathbf{f} \quad (3.25)$$

Here, the vector  $\mathbf{u}_p$  contains the radial and vertical displacement of the shell and  $\mathbf{u}_s^j$  contains the radial and vertical displacement in soil layer  $j$ . The matrices  $\mathbf{L}$  and  $\mathbf{I}$  are the stiffness and inertia matrices respectively. The vector  $\mathbf{t}_s^j$  represents the stress in soil layer  $j$  surrounding the pile and  $\mathbf{p}_f$  is the surrounding pressure in the water-column. The force that is applied by the hammer is represented by the vector  $\mathbf{f}$ . The vector notations are described in the following equations.

$$\mathbf{t}_s^j = [\lambda_j \nabla \cdot \mathbf{u}_s^j \mathbf{I} + \mu_j (\nabla \mathbf{u}_s^j + (\nabla \mathbf{u}_s^j)^T)] \cdot \hat{\mathbf{r}} \quad (3.26)$$

$$\mathbf{f} = [f_{rz}(z, t), f_{rr}(z, t)]^T \quad (3.27)$$

$$\mathbf{u}_p = [u_{p,z}(z, t), u_{p,r}(z, t)]^T \quad (3.28)$$

$$\mathbf{u}_s^j = [u_{s,z}(r, z, t), u_{s,r}(r, z, t)]^T \quad (3.29)$$

The pile extension is modelled as rigid baffle below the pile. This is such that the soil below the pile tip can be extended such that the reflection of the rigid boundary has less effect. A transformation to the frequency domain yields the following equation:

$$\mathbf{L}\tilde{\mathbf{u}} + \tilde{\mathbf{I}}\tilde{\mathbf{u}} = (H(z - z_1) - H(z - L))\tilde{\mathbf{t}}_s - (H(z - z_0) - H(z - z_1))\tilde{\mathbf{p}}_f + \tilde{\mathbf{f}} \quad (3.30)$$

The tilde denotes that the quantity is a complex value.

### 3.2.2 Fluid domain

The motion in the fluid domain, as mentioned in section 3.1, can be described by the Helmholtz equation (3.31). Tsouvalas (2015) described the motion by a scalar velocity potential in a cylindrical coordinate system. This is valid in the domain  $z_0 \leq z \leq z_1$  and  $r \geq R$ .

$$\nabla \tilde{\phi}_f(r, z, \omega) + \frac{\omega^2}{c_f^2} \tilde{\phi}_f(r, z, \omega) = 0 \quad (3.31)$$

The solution to equation 3.31, which is based on the separation of variables (Tsouvalas, 2015) (see 3.1.1), is given in (3.32). The Hankel function solves the the radiation condition at  $r \rightarrow \infty$ .

$$\tilde{\phi}(r, z, \omega) = H_0^{(2)}(k_{\phi,r}) (A_1 e^{-\alpha_f z} + A_2 e^{\alpha_f z}) \quad (3.32)$$

Here,  $k_{\phi,f}$  is the separation constant and  $\alpha_f$  is calculated as  $\sqrt{k_{\phi,f}^2 - \omega^2/c_f^2}$ . In which  $c_f$  is the phase velocity of the waves in the fluid.  $A_1$  and  $A_2$  are complex constants, which are determined by the boundary and interface conditions.

### 3.2.3 Soil domain

Tsouvalas (2015) also described the motion of the soil layers. Note that this is valid for multiple layers. In the case of this research. Two layers are modelled. The equation of motion of the soil is transformed into the frequency domain, yielding equation 3.33.

$$\mu_{s,j} \nabla^2 \tilde{\mathbf{u}}_s^j + (\lambda_{s,j} + \mu_{s,j}) \nabla \nabla \tilde{\mathbf{u}}_s^j + \omega^2 \rho_{s,j} \tilde{\mathbf{u}}_s = 0 \quad (3.33)$$

This is valid for the domain  $z_1 \leq z \leq L$  and  $r \geq R$

By applying  $\tilde{\mathbf{u}}_s = \nabla \tilde{\phi}_s + \nabla \times \tilde{\boldsymbol{\psi}}_s$ , Tsouvalas (2015) finds a solution for the velocity and displacement potentials  $\tilde{\phi}_s$  and  $\tilde{\boldsymbol{\psi}}_s$  based on the separation of variables method. The Hankel functions in the solution satisfy the radiation condition at  $r \rightarrow \infty$ .

$$\tilde{\phi}_s(r, z, \omega) = H_0^{(2)}(k_{\phi,s}) (A_3 e^{-\alpha_s z} + A_4 e^{\alpha_s z}) \quad (3.34)$$

$$\tilde{\boldsymbol{\psi}}_s(r, z, \omega) = H_1^{(2)}(k_{\psi,s}) (A_5 e^{-\beta_s z} + A_6 e^{\beta_s z}) \quad (3.35)$$

Here,  $k_{\phi,s}$  and  $k_{\psi,s}$  are the separation constants and  $\alpha_s$  and  $\beta_s$  are defined as:

$$\alpha_s = \sqrt{k_{\phi,s}^2 - \omega^2/c_L^2} \quad (3.36)$$

$$\beta_s = \sqrt{k_{\psi,s}^2 - \omega^2/c_T^2} \quad (3.37)$$

In which  $c_L$  and  $c_T$  are the compressional and shear wave speed respectively.  $A_3$ ,  $A_4$ ,  $A_5$  and  $A_6$  are complex constants which are to be determined by the boundary and interface conditions.

### 3.2.4 Boundary and interface conditions

Within the solid and fluid domain, boundary conditions need to be considered to calculate the undetermined complex coefficients  $A_1..A_6$ . To couple the different media and the pile, interface conditions are added as well. First the following boundary conditions apply:

- Radiation condition at  $r \rightarrow \infty$
- Pressure release surface at  $z = z_0$
- Rigid bottom at  $z = D$

The radiation condition is already applied in the equations 3.32, 3.34 and 3.35 by terms of the Hankel functions. The pressure release surface is stated as follows:

$$\tilde{p}_f(r, z_0, \omega) = 0, r \geq R \quad (3.38)$$

The rigid boundary at the bottom is defined in the following manner.

$$\tilde{u}_{s,r}(r, D, \omega) = \tilde{u}_{s,z}(r, D, \omega) = 0, r \geq R \quad (3.39)$$

Next, the four interface conditions are identified by Tsouvalas (2015). The first condition being the interface between the first soil layer and the fluid layer. Second is the interface between the subsequent soil layers. Finally, the interface conditions between the pile and the water column and the pile and soil domain was identified

The interface between the upper soil layer and fluid layer states how the stresses ( $\sigma$ ) and displacements ( $u$ ) in the soil interact with the pressure and particle velocity in the water column. Equation 3.40 states that the out-of-plane vertical stress induces a pressure in the watercolumn. Equation 3.41 shows that that in-plane stress in r-direction does not influence the watercolumn, since a fluid does not has have a shear stress component. Equation 3.42 shows the relation between the soil displacement and the velocity ( $v$ ) that is induced by it.

$$\tilde{\sigma}_{s,zz}(r, z_1, \omega) + \tilde{p}_f(r, z_1, \omega) = 0, r \geq R \quad (3.40)$$

$$\tilde{\sigma}_{s,zr}(r, z_1, \omega) = 0, r \geq R \quad (3.41)$$

$$\tilde{u}_{s,z}(r, z_1, \omega) - \frac{\tilde{v}_{f,z}(r, z_1, \omega)}{i\omega} = 0, r \geq R \quad (3.42)$$

Next are the interface conditions between the (j+1)th and jth soil layer. These interface conditions describe that the stress (3.43)..(3.44) and displacement (3.45)..(3.46) in layer (j+1) and layer j must be the same.

$$\tilde{\sigma}_{s,zz}^{j+1}(r, z_j, \omega) - \tilde{\sigma}_{s,zz}^j(r, z_j, \omega) = 0, r \geq R \quad (3.43)$$

$$\tilde{\sigma}_{s,zr}^{j+1}(r, z_j, \omega) - \tilde{\sigma}_{s,zr}^j(r, z_j, \omega) = 0, r \geq R \quad (3.44)$$

$$\tilde{u}_{s,z}^{j+1}(r, z_j, \omega) - \tilde{u}_{s,z}^j(r, z_j, \omega) = 0, r \geq R \quad (3.45)$$

$$\tilde{u}_{s,r}^{j+1}(r, z_j, \omega) - \tilde{u}_{s,r}^j(r, z_j, \omega) = 0, r \geq R \quad (3.46)$$

Finally, the interface conditions between the pile and the fluid-soil interface are considered. Here, a non-slip condition between the pile wall and soil-fluid domain is assumed. The interface conditions state how the displacement of the pile is coupled to the velocity in the fluid (3.47) and the displacement in the soil.

$$\tilde{u}_{p,r}(z, \omega) - \frac{\tilde{v}_{f,r}(R, z, \omega)}{i\omega} = 0, z_0 < z < z_1 \quad (3.47)$$

$$\tilde{u}_{p,r}(z, \omega) - \tilde{u}_{s,r}(R, z, \omega) = 0, z_1 < z < L \quad (3.48)$$

$$\tilde{u}_{p,z}(z, \omega) - \tilde{u}_{s,z}(R, z, \omega) = 0, z_1 < z < L \quad (3.49)$$

In this section, the governing equations and boundary- and interface conditions are shown for the SILENCE near field model. These equations are based on the work of Tsouvalas (2015) and Tsouvalas (2020). The full vibro-acoustic problem is described by equations (3.30), (3.32), (3.34) and (3.35) together with the boundary and interface conditions (3.38) ... (3.49) (Tsouvalas, 2015).

### 3.3 SILENCE Far field model

As mentioned in the previous section, the near-field module contains a rigid boundary condition (3.39). This can lead to a reflective waves channeling the energy back into the water column. It is important to emphasize that this reflection is not realistic. For this reason, the SILENCE near field model can simulate up to a certain range, depending on how deep the rigid boundary condition lies. Please note that the deeper the rigid boundary condition is, the more costly the computation is. As a solution to this problem, the near field solution is used as source in the far field model where this rigid boundary condition is not present. In this section a brief description of the far-field module is described based on the work of Peng, Tsouvalas, and Metrikine (2019) and Peng, Tsouvalas, and Metrikine (2020).

First of all, the far-field module aims to propagate the wave field which is generated in the near field module (Peng, Tsouvalas, and Metrikine, 2019). In principal, the far field model works as follows. To overcome problem with the rigid boundary condition, the far field module includes a half-space for the deepest boundary.

Under the assumption that a ring source is positioned at  $(r_0, z_0)$ (fig. 3.5), the acoustic field in frequency domain can be described for the three potential functions  $\tilde{\phi}_f$  (Displacement potential in the fluid),  $\tilde{\phi}_s$  (Compressional displacement potential in the soil) and  $\tilde{\psi}_s = [0, \tilde{\psi}_s, 0]^T$  (shear potential in the soil). The equation of motion in the frequency domain is described as follows:

$$[\nabla^2 + k_\xi^2]\tilde{G}(r, z; r_0, z_0, \omega) = \frac{\delta(r - r_0, z - z_0)}{2\pi r} S_\xi(\omega) \quad (3.50)$$

For which,  $\tilde{G}(r, z; r_0, z_0, \omega)$  stands for Green's function that describes the solution for the aforementioned displacement potentials.  $k_\xi$  denotes the medium wavenumber, of which  $\xi$  denotes the type of source (f = fluid source, p = compressional source and s = shear source). Finally,  $S_\xi(\omega)$  describes the source strength of the impulse denoted by the delta function located at  $(r_0, z_0)$ .

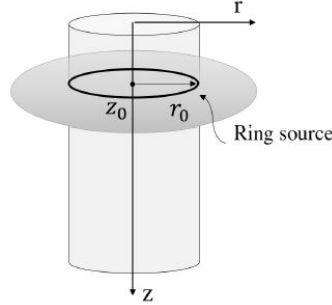


Figure 3.5: Ring source in cylindrical coordinates (Tsouvalas, 2020)

When equation 3.50 is transformed in the Hankel domain, the following depth separated equation is found.

$$\left[ \frac{d^2}{dz^2} + k_{z,\xi}^2 \right] \hat{G}(k_r, z; r_0, z_0, \omega) = \frac{J_0(k_r r_0)}{2\pi} \delta(z - z_0) S_\beta^\xi(\omega) \quad (3.51)$$

Here,  $\beta$  denotes the direction at source point  $(r_0, z_0)$ .

After finding a solution for  $\hat{G}(k_r, z; r_0, z_0, \omega)$ , the inverse Hankel transform is applied to (3.51).

$$\tilde{G}(r, z; r_0, z_0, \omega) = -\frac{1}{2} \int_{-\infty}^{\infty} \left( S_\beta^\xi(\omega) \frac{e^{-ik_{z,\xi}|z-z_0|}}{4\pi i k_{z,\xi}} + A_\xi^1 e^{ik_{z,\xi}z} + A_\xi^2 e^{-ik_{z,\xi}z} \right) \cdot J_0(k_r r_0) H_0^{(2)}(k_r r) k_r dk_r \quad (3.52)$$

As indicated earlier, the radiation condition in z-direction must be taken into account at the soil half-space located in the domain  $z > z_N$ . This is simply done by applying  $A_\xi^1 = 0$  for  $z \geq z_N$ . This means that a downward propagating wave leaves the domain without any reflection. Like in the near-field module, the boundary and interface conditions (3.38)..(3.46) apply to the far-field module as well. If (3.52) is substituted in these conditions, a system of linear algebraic equations is found. These can be solved for coefficients  $A_\xi^1$  and  $A_\xi^2$ . When the solution is found to these amplitudes, the Green's function for the complete field can be obtained. For the evaluation of the integral given in (3.52) the reader is referred to (Peng, Tsouvalas, and Metrikine, 2020).

After deriving the expression for the Green's functions, the next step is to couple the near-field module to the far-field module. This is done by means of a boundary element method (BEM) which is discussed in a brief manner<sup>1</sup>.

From the derived Green's potential functions  $\tilde{\phi}_f^g$ ,  $\tilde{\phi}_s^g$  and  $\tilde{\psi}_s^g$ , the displacement tensor  $\tilde{U}_{\alpha\beta}^{\Xi\xi}$  is derived at receiver point  $(r, z)$  in medium  $\Xi$  in direction  $\alpha$  as a result

<sup>1</sup>For a detailed description the reader is referred to (Peng, Tsouvalas, and Metrikine, 2020) and (Tsouvalas, 2020)



- Scenario 3: Test with AdBm + BBC
- Scenario 4: Test with BBC only

For this research, scenario 1 and scenario 4 are of importance. Scenario 1 is used for validation and scenario 4 is used to compare the simulations, involving a BBC. Note that scenario 4 also applies to the other monopiles, since those are installed regularly. The measurements were taken in four directions and distances 750, 1500 and 5000 m (figure 3.6). Every measurement beacon consisted of two hydrophones, one hydrophone at 2 m from the seabed and one 10 m from the seabed. The hydrophones have a measurement accuracy of  $<2$  dB resp.  $\pm 1$  dB. (Bellmann, 2019).

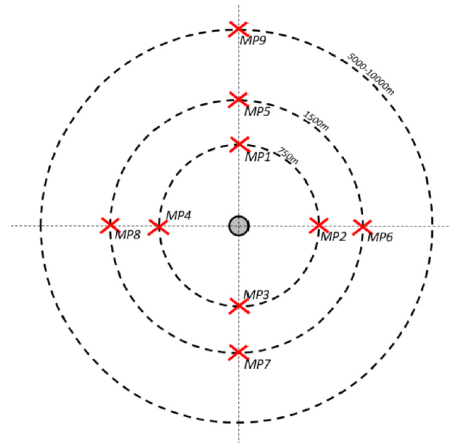


Figure 3.6: Schematic top overview of the measurement set-up (Elzinga et al., 2019)

The data that are selected for validation are based on the following criteria. The first criterion is that noise mitigation should be absent during the measurement in order to study the generation and propagation of sound. The second criterion is that the SILENCE model assumes a constant bathymetry. Therefore, it is desirable to select a location with with a bathymetry that is as uniform as possible. This choice is based on the fact that sand waves could influence the measurement data, since sand waves reflect noise due to an impedance mismatch (Jensen et al., 2011). Usually the hydrophone is placed at 2m from the seabed. It is possible that hydrophones are placed behind a sandwave, thus record less noise.

The measurements without noise mitigation are performed on [REDACTED] of which [REDACTED] proved to be the measurement with the flattest bathymetry. That is for the measurements in north-east direction and south-west direction (see appendix A). The hydrophones associated with these directions are MB1, MB3, MB5 and MB7. For the validation the measurements at 750m were used. The choice is made to perform the simulation in a duration of 0.75 seconds. In this time frame, the noise at 750m can be calculated. However, calculating the noise levels at larger distances requires a longer duration. Therefore, the validation is performed by comparing the simulation to the measurements at 750m.

### 3.4.2 Model input data

#### Force input

In SILENCE, the hammer blow is modelled as a vertical force (Tsouvalas, 2015). For the validation analysis, the forcing function is also approximated due to the lack of hammer force data. The forcing function used in this research is a modified equation based on the work of Lippert, Nijhof, et al. (2016). This force type has a sharp peak which is not realistic, it is also common to use a smooth exponential function (Tsouvalas, 2015).

$$F(t) = \begin{cases} 0 & \text{for } t < t_0 \\ \frac{F_p}{t_r}(t - t_0) & \text{for } t_0 \leq t < t_0 + t_r \\ F_p \exp\left(\frac{t - (t_r + t_0)}{t_d}\right) & \text{for } t \geq t_0 + t_r \end{cases} \quad (3.56)$$

The numerical values that are used for the forcing function are shown in table 3.1. These values are iteratively chosen based on whether the SILENCE output matches the ██████ data, note that this cannot be calculated beforehand. Primarily the energy input must match the measured blow energy, in this case at full penetration. The blow energy and sound levels depend on the magnitude and the duration of the pulse. This can be changed with parameter  $t_r$  and  $t_d$ . The forcing function is shown in figure 3.7.

Variable	Value	Unit
$F_p$	210	MN
$t_0$	0.01	s
$t_r$	0.002	s
$t_d$	0.004	s

Table 3.1: Variables for forcing function

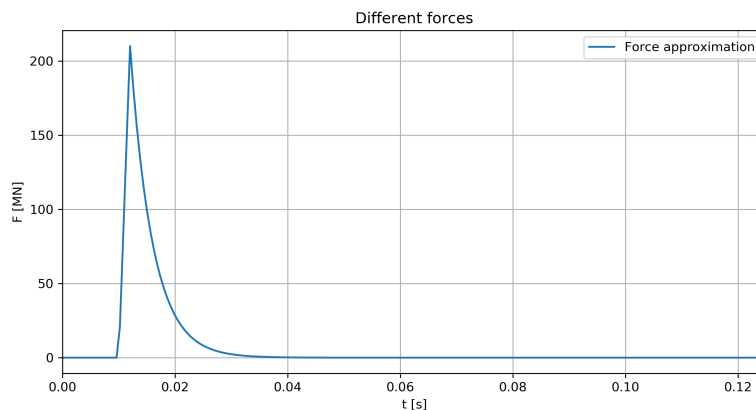


Figure 3.7: Force approximation based on the work of Lippert, Nijhof, et al. (2016)

Additionally, a frequency analysis is performed on this forcing function by applying the Fourier transform (3.57).

$$F(\omega) = \int_{-\infty}^{\infty} F(t)e^{-i\omega t} dt \quad (3.57)$$

It is important to analyze the frequencies that make up the forcing function. The frequency analysis must show that the magnitude (and thus energy) of the forcing function in frequency domain decays to zero at higher frequencies. It is important to prove this because then it can be assumed that most energy from the blow is taken into account when solving the vibro-acoustic problem in frequency domain. Note that the forcing is an approximation and that real forces are of more complex nature, resulting in higher frequencies (order of magnitude  $\geq 5$  kHz). Solving for these high frequencies takes more computational time and is not necessary since the main frequencies due to piling are between 31.5 and 800 Hz (Elzinga et al., 2019).

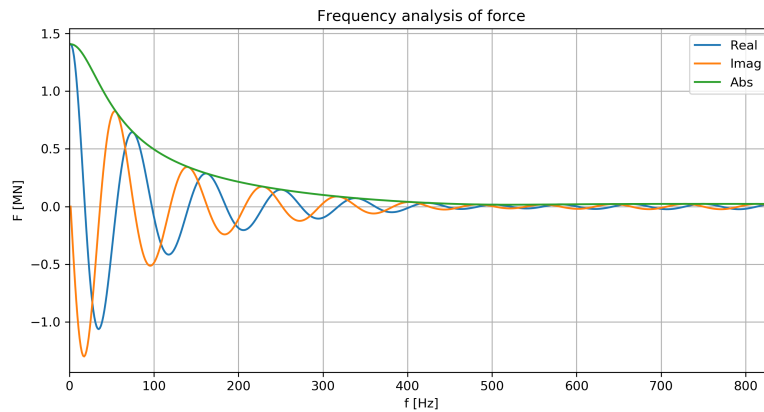


Figure 3.8: Frequency analysis showing that the energy decays to zero at high frequencies

From a numerical perspective, the forcing function is discretized. The way it is discretized, determines the maximum number of frequencies that are used in the calculation. The forcing function has a duration of  $T_{max}$  and a time step  $\Delta t$ . These determine the frequency step  $\Delta f$  and the maximum frequency  $f_{max}$ . The frequency step  $\Delta f$  is calculated by  $\Delta f = \frac{1}{T_{max}}$ . The maximum frequency is calculated by  $f_{max} = \frac{1}{2\Delta t}$

Variable	Value	Unit
$\Delta t$	0.0006	s
$T_{max}$	0.75	s
$N_t$	1000	-
$\Delta f$	1.3333	Hz
$f_{max}$	833.3333	Hz
$N_f$	625	-

Table 3.2: Stepsize, maximum and amount of the time and frequency vectors

### Pile geometry and properties

Monopiles are generally built of multiple sections which have different wall thicknesses. Additionally, the diameter of the monopile varies on the top half, giving it a conical shape at the top. For the simulation a straight monopile is assumed with a constant wall thickness. For the diameter, the largest section diameter is chosen because this diameter is valid for approximately 50% of the pile. However, the wall thickness varies in almost every section. Therefore, the choice is made to average the wall thickness over the number of sections according to equation 3.58. Here,  $n$  is the section number,  $N$  the total number of sections and  $t_n$  the thickness of a section.

$$\overline{t_{wall}} = \frac{1}{N} \sum_{n=1}^N t_n \quad (3.58)$$

For [REDACTED], the average wall thickness is chosen at [REDACTED] and the diameter is chosen at [REDACTED]. The length of the pile is naturally based on the technical specifications of the monopile. The length of [REDACTED] is [REDACTED]. The input parameters for the monopile are summarized in table 3.3.

Variable	Value	Unit
$\rho_s$	7850	kg/m <sup>3</sup>
$\nu_s$	0.28	-
$E_s$	2.10E+11	N/m <sup>2</sup>
$D_{pile}$	[REDACTED]	m
$L_{pile}$	[REDACTED]	m
$\overline{t_{wall}}$	[REDACTED]	m

Table 3.3: Input parameters monopile

### Water column

The water column has properties density ( $\rho$ ) and compressional wave speed ( $c_f$ ). For the validation, it is assumed that the water column has a constant density and compressional wave speed over the entire column. The assumed density is 1000 kg/m<sup>3</sup> and an assumed wave speed of 1500 m/s is used in the validation.

### Soil layering and properties

At the location of [REDACTED], a cone penetration test (CPT) was performed up to [REDACTED] below the seabed (figure 3.9). From the CPT's, several layers were determined of which the majority can be referred to as a [REDACTED]. The monopile [REDACTED] penetrates the soil [REDACTED] deep. This means that 80% of the soil in which the pile is situated is [REDACTED] and 20% is [REDACTED]. Note that this is qualitatively derived from figure 3.9. In SILENCE, the soil layering consists of two soil layers. Because the majority of the energy, that influences the water column, flows through the upper layers of the soil (Tsouvalas, 2015), the two layers in SILENCE are modelled as [REDACTED]. Layer 1 is modelled based on the properties of the [REDACTED] (green layer in figure 3.9) and layer two is modelled based on an average of the

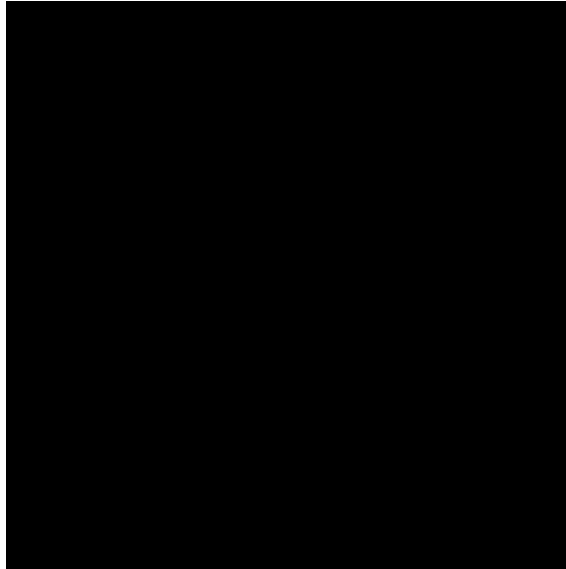


Figure 3.9: Censored for confidentiality

properties of the [REDACTED] (blue, grey and light purple layers in figure 3.9 respectively).

The domain is defined in  $z_2 \leq z \leq z_{bedrock}$  as shown in figure 3.4. In reality, soil contains more layers. So in order to model the soil, some assumptions are needed. The interface between the soil layers ( $z_2$ ) is placed such that the first soil layer is modelled according to the CPT report and the properties of the layers below are averaged. Furthermore, the interface is also placed at a position such that the pile penetrates both layers. Figure 3.10 shows how the layers are placed in relation to the pile. Note that the levels are measured from the top of the pile.

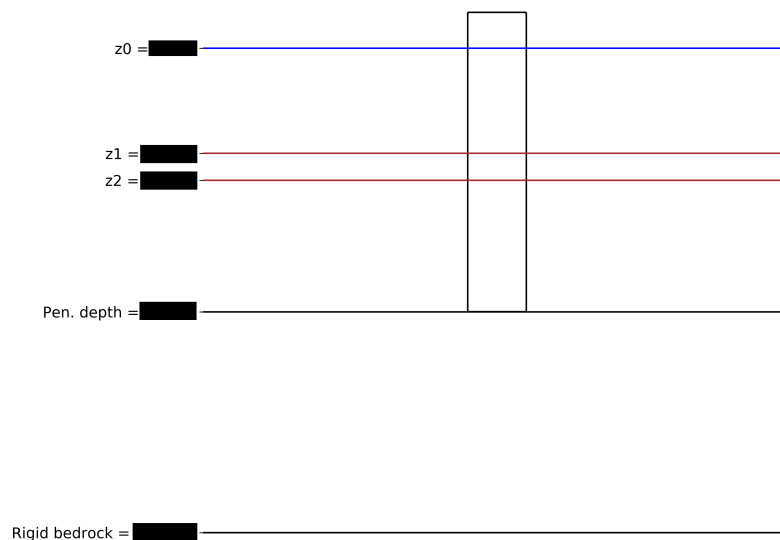


Figure 3.10: Soil layering in SILENCE

The SILENCE model requires three inputs for the soil data, density ( $\rho$ ), Poisson ratio ( $\nu$ ) and Young's modulus ( $E$ ). The assumptions are checked by looking at the shear wave speed ( $c_T$ ) and compressional wave speed ( $c_L$ ). For clay and sand layers,

the magnitude of the shear wave velocity is between 100 and 500 m/s (Aziman et al., 2016). The compressional wave velocity is between 300 and 1900 m/s (Aziman et al., 2016).

The magnitude of the required parameters is based on calculations from the CPT report provided by Van Oord. The calculations provide the bulk unit weight of the soil ( $\gamma_s$ ), the Young's modulus ( $E$ ), a poisson's ratio ( $\nu$ ) and small strain shear modulus ( $G_0$ ). The Poisson ratio  $\nu$  is recommended to be 0.5 for undrained conditions. However, since this yields a division by zero in equation 3.59, a slightly lower approximation is used. This approximation is iteratively checked with equation 3.60 and compared with the magnitudes by Aziman et al. (2016).

$$\lambda = \frac{2\mu\nu}{1 - 2\nu} \quad (3.59)$$

$$c_L = \sqrt{\frac{\lambda + 2\mu}{\rho}} \quad (3.60)$$

The required parameters are summarized in 3.4. These values are deemed to be realistic based on the calculated shear and compressional wave velocities and the magnitudes by Aziman et al. (2016).

<b>Soil layer 1:</b>		
$z_1 \leq z \leq z_2$	████████████████████	m
$\rho_{soil,1}$	████████	kg/m <sup>3</sup>
$\nu_{soil,1}$	██████████	-
$E_{soil,1}$	████	MPa
$c_{s,1}$	██████████	m/s
$c_{p,1}$	██████████	m/s
$\alpha_{p,1}$	██████	-
$\alpha_{s,1}$	██████	-
<b>Soil layer 2:</b>		
$z_1 \leq z \leq z_{rigid}$	████████████████████	m
$\rho_{soil,2}$	████████	kg/m <sup>3</sup>
$\nu_{soil,2}$	██████████	-
$E_{soil,2}$	██████	MPa
$c_{s,2}$	██████████	m/s
$c_{p,2}$	██████████	m/s
$\alpha_{p,2}$	██████	-
$\alpha_{s,2}$	██████	-

Table 3.4: Input parameters soil

### 3.4.3 Validation results

Here, the noise prediction is presented for validation of the SILENCE model. The measurement data was obtained at the █████ OWF at 2 meters from the seabed at 750m from the pile. First, the input energy is shown. This input energy was calculated such that it is in agreement with the measurement data. Secondly, the frequency spectra are shown. Here, the sound exposure level per frequency is compared to the measurement data and the evolution of the spectra over distance is shown. Thirdly, the evolution of the pressure in time is shown. This was simulated 5m from the sea surface and 2m from the seabed at various distances. Finally, the SEL and  $L_{p,pk}$  are presented as a function of distance from the pile. Here, a comparison with the measurements is shown.

#### Input energy

The input energy is the primary quantity to check when comparing simulation results to measurement data. This is because the energy that is going into the system depends on the dynamic response of the structural system. The parameters that play a role in this are pile diameter, thickness, penetration depth, soil layering, soil properties and input force. The total energy in the system cannot be calculated beforehand. To calculate the energy flux and finally the total energy, the velocity and force at a certain location needs to be known. This is only known when the response is found. Based on the cumulative energy per cross section, an estimation of the input energy can be made (Figure 3.11). Note that the wavy pattern in this figure is an artefact of the modal sum<sup>2</sup>. The input energy is more or less the average of the wave pattern up to the pile length (red line). The calculated input energy in this case was █████ kJ. In reality the recorded blow energy was █████ kJ.

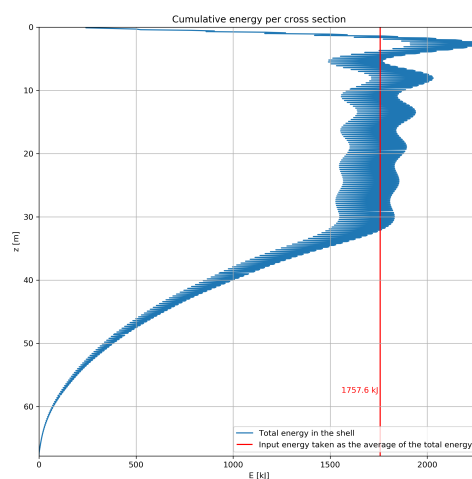


Figure 3.11: Cumulative energy per cross-section

<sup>2</sup>The solution of a problem consists of an infinite number of modes. Because this is computationally not possible, the modes are truncated, leading to artefacts in the output.

### Frequency spectrum

In order to compare the sound exposure per frequency bin, SEL spectra are determined. This is presented in 1/3 octave bands. Figure 3.12 shows a comparison of the 1/3 octave SEL simulated at 750m and a 1/3 octave SEL from the ITAP report (Bellmann, 2019). Note that due to the lack of frequency spectra per blow, the measurement that is shown is the median of all the recorded blows. Therefore it is lower than the simulated spectrum. However, it does show the same trend. Figure 3.13 shows the evolution of the frequency spectra over distance. Here, a decrease in SEL per frequency is observed for the entire bandwidth. Higher frequencies tend to decay faster than low frequencies. Furthermore, the sound exposure level decay rate decreases over distance.

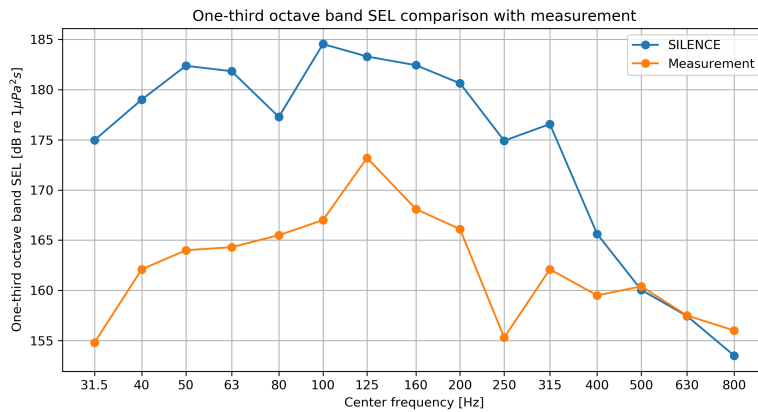


Figure 3.12: Frequency spectrum compared with measurements at 750m

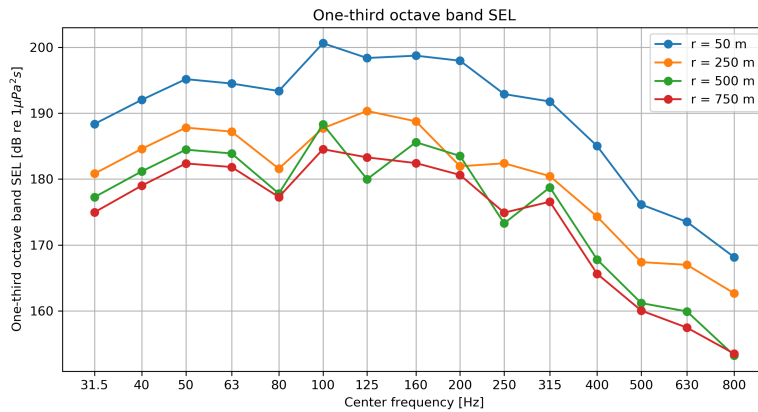


Figure 3.13: Evolution of the noise 1/3 octave band SEL spectrum

### Time domain solution

Figure 3.14 shows the evolution of the pressure measurements at various distances from the pile. It is shown for a hydrophone placed 5m below the surface and 2m above the seabed. A distinct peak is observed in the pressure recording. A rough approximation of the arrival time at 750m ( $t = c_w/r_{hf} = 1500/750 = 0.5s$ ) shows that the simulation is in good agreement with this. This also applies to the other distances that are plotted in the figure.

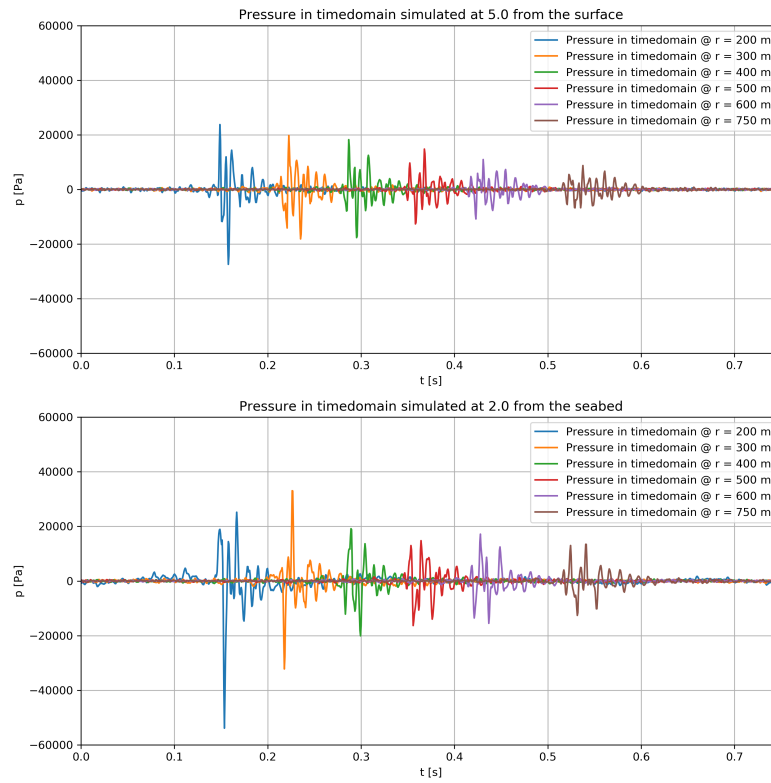


Figure 3.14: Evolution of the pressure in time and space

### Comparison to measurement data

The next step in validation of the model is to compare the simulation results to the measurement data. As can be seen in figure 3.15, responses have been simulated for from 10 m up to 750 m with steps of 10 m. At 750m from the pile, the simulated SEL and  $L_{p,pk}$  fit within the range of the data. Specifically, the calculated SEL and  $L_{p,pk}$  deviate 1.7 dB and 2.2 dB from the mean respectively. A difference in trend between SEL and  $L_{p,pk}$  is observed. This is because  $L_{p,pk}$  is more susceptible to local constructive and destructive interference of the waves.

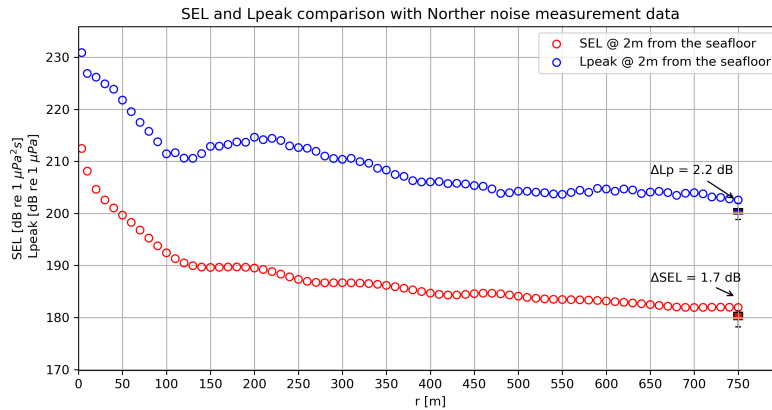


Figure 3.15: Comparison of simulation vs. measurement SEL and  $L_{p,pk}$ . Note that the internationally standard symbol for peak pressure ( $L_{p,pk}$ ) is denoted as  $L_{peak}$  in the figure.

### 3.4.4 Energy and spectra near the seabed

Here, the energy flux in z-direction (fig. 3.16) and r-direction (fig. 3.17) are presented. The energy flux in the z-direction is presented in normalized form. It indicates which layer channels the most energy. Figure 3.16 shows that most energy flows through the upper soil layer. It is also observed that energy in the water column grows rapidly near the sea floor.

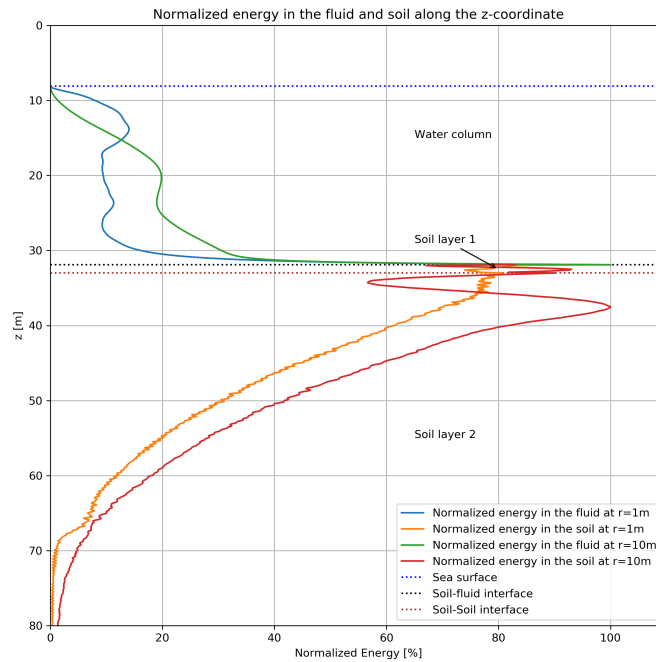


Figure 3.16: Normalized energy flux along the z-coordinate for various distances from the pile's surface

To indicate where the most energy leaks in the water column, figure 3.17 is shown. Here, it can be observed that in the vicinity of the pile, there is a significant amount of leakage, which decays over distance. This is done by calculating the energy at 0.1m above the seabed for various distances from the pile's surface up to 150m. It can be observed that an energy transfer is present over the entire distance. Moving the bubble curtain may indicate which distance this is significant. Figure 3.18 indicates that the frequency content near the seabed is dominated by low frequencies.

#### Influence of the hammer force on the energy radiation

Figure 3.19 shows how the amplitude of the hammer force affects the energy radiation in the water column. The base case for this analysis was an amplitude of 210MN. It was compared to a 20% higher and 20% lower force. In figure 3.19 a linear increase and decrease is observed for the harder and softer blow respectively.

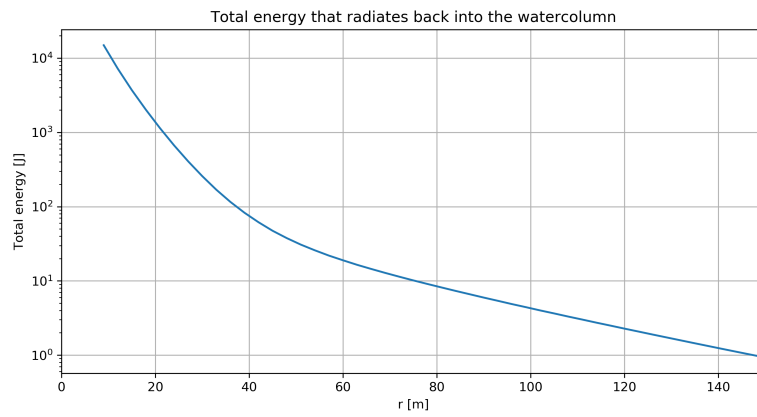


Figure 3.17: Total energy that radiates back in the water column

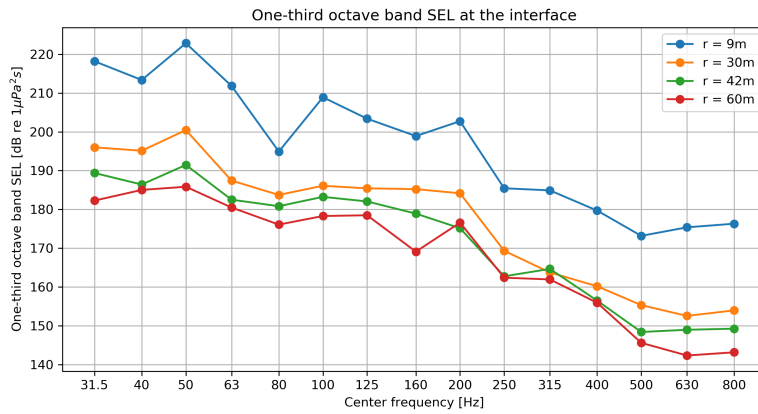


Figure 3.18: Frequency spectra 0.1m from the seabed

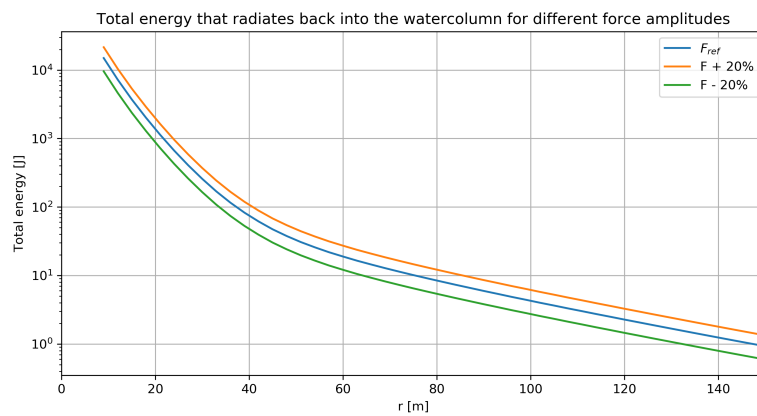


Figure 3.19: Effect of the force amplitude on the energy radiated into the water column



# Chapter 4

## Bubble curtain implementation

This chapter discusses the modeling strategy of the bubble curtain. First, an in depth overview is given on the working principles of a bubble curtain in section 4.1. Next, the modeling strategy is explained in section 4.2. Finally, three different scenarios are shown in section 4.4.

### 4.1 The noise reduction by a bubble curtain

In section 2.3 the working mechanisms of a bubble curtain are briefly discussed. In this section a closer look is presented at the damping characteristics of the bubble curtain. Ultimately, it is explained which effects have been modeled and ignored, including their effects.

#### 4.1.1 Noise reduction mechanisms

Primarily, the noise reduction of a bubble curtain is determined by two effects. The first effect is the reflection of the sound waves by an impedance mismatch between the sea water and the bubble cloud. The second effect in which damping takes place is due to resonance of the bubbles as the sound waves travel through the bubbly medium. These two mechanisms were investigated experimentally by Rustemeier, Griebmann, and R. Rolfes (2012). They concluded that a dense layer of slow rising bubbles of small radii improves noise reduction compared to the same air-volume content with less larger bubbles.

Figure 4.1 shows the sound exposure level spectra obtained at the █████ OWF. It shows a distinct peak between 63 and 500 Hz. Such low frequencies require a bubble size range of 8 - 32mm near the sea surface and 14 - 50mm at a depth of 30m (Tsouvalas, 2020). Creating such large bubbles under offshore conditions is difficult because the bigger the bubbles the more unstable they are. Although the bubble resonance may have an effect, the impedance mismatch between the bubbly layer and the water is governing (Tsouvalas, 2020). Therefore, the thickness of the bubble curtain and the air concentration are governing for the effectiveness of the bubble curtain. This can be controlled by following parameters (Diederichs et al., 2014):

- Air flow
- Nozzle diameter

- Nozzle spacing
- Space between curtains in case of a DBBC

In figure 4.1, the noise reduction per octave band can be seen. The red dotted line indicates the measurements where a BBC is applied. It shows that the noise transmission is frequency dependant. The noise at low frequency range ( $\leq 125\text{Hz}$ ) is reduced less compared to high frequency noise.

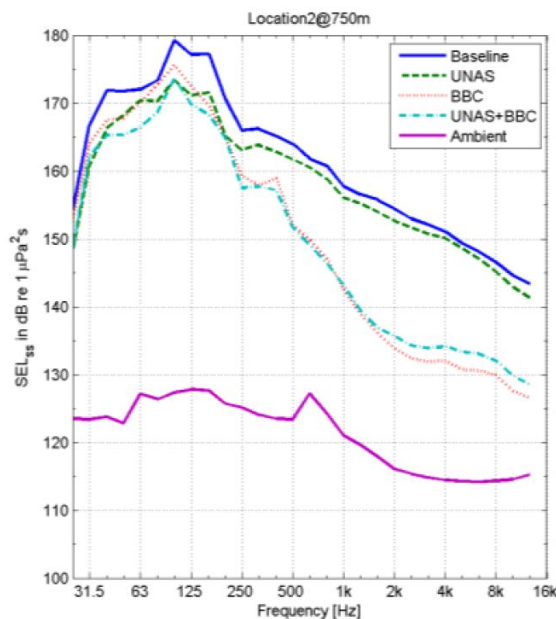


Figure 4.1: SEL Octave band spectra from the measurements, showing a baseline measurement without noise mitigation next to three different noise mitigation set-ups (Elzinga et al., 2019)

### 4.1.2 The influence of currents

Currents are usually present in offshore conditions. They can influence the shape of the bubble curtain and also the uniformity of the bubble curtain. It is expected that currents influence the effectiveness of the noise reduction but those are left out of the scope of this thesis.

### 4.1.3 Distance of the bubble curtain

Another influence on the mitigation of noise is the location of the BBC. As discussed in chapter 2, a large contribution to underwater noise is the Mach cone generated by the radial expansion of the steel due to the compressional wave traveling at supersonic speed vertically along the pile after the impact. This primary noise path can mostly be mitigated by the bubble curtain. When the compressional wave in the pile is reflected, an upward Mach cone is created. This Mach cone radiates back in the water column. Figure 4.2 shows what happens when the bubble curtain is placed close to the pile (I.). In this case the upward-going Mach cone will travel underneath the bubble curtain and back in the water column behind the BBC.

This can be prevented by placing the bubble curtain further from the pile (II.). This location is governed by the angle of the upward moving Mach cone, which is determined by the properties of the soil.

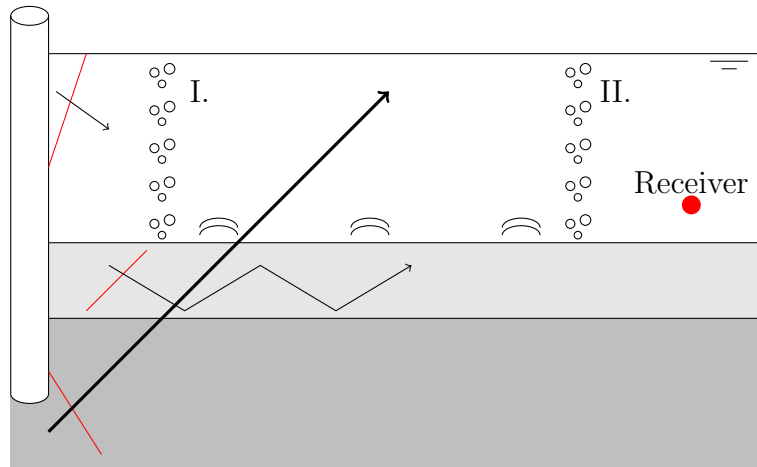


Figure 4.2: Schematic representations of noise paths, compared to the bubble curtain and receiver location

Seismic waves, which contain body and interface waves, also play a role in determining the bubble curtain location. In the upper layer, noise is tunneled often because upper layer is almost fluid of nature. This 'tunneling effect' might leak noise back into the water column. This energy leakage cannot be reduced by the bubble curtain. Theoretically, if the bubble curtain is placed as close to the receiver as possible, the noise leakage will be blocked by the bubble curtain. However, receivers are legally placed at 750m. For such a radius, a hose with length  $\approx 4.7\text{km}$  is needed. Besides that this is impractical, it is also very expensive. Ultimately, it is expected that a bubble curtain location far from the source results in better noise reduction. However, simulations must provide insight on what a practical location is.

## 4.2 The effective source reduction approach

To examine the noise reduction by a bubble curtain, an effective source reduction strategy is performed in combination with the SILENCE model. This strategy has the following steps:

1. Generate the source with the SILENCE Near-Field module<sup>1</sup>;
2. Reduce the noise level at the location of the air bubble curtain system by applying a depth- and frequency dependent source reduction factor;
3. Propagate the wave field with the SILENCE Far-Field module.

<sup>1</sup>When the SILENCE near-field model is used as input for the source reduction model, the rigid boundary was lowered which results in longer computation time. A faster approach is to use the propagation module as input for the source reduction model. This is further discussed in the section 6.2.

This strategy does not include the current nor the resonance effect of the bubbles. However, the distance of the bubble curtain as well as the frequency dependent transmission is considered.

The attenuation of the amplitude of the pressure and velocity spectrum is performed by multiplying the SILENCE Near-Field output ( $P(\omega, z)$ ) by a coefficient matrix ( $M(\omega, z)$ ) at the location of the bubble curtain ( $r_{bc}$ ).

$$P(\omega, z)^* = P(\omega, z)\mathbf{M}(\omega, z) \quad (4.1)$$

$$V_r(\omega, z)^* = V_r(\omega, z)\mathbf{M}(\omega, z) \quad (4.2)$$

$$V_z(\omega, z)^* = V_z(\omega, z)\mathbf{M}(\omega, z) \quad (4.3)$$

Here,  $M_{i,j}$  consists of transmission coefficients which are depth and frequency dependant. The frequency dependence follows from a transmission coefficient (4.5) formulated by Commander and Prosperetti (1989). Here,  $s$  is the thickness of the bubble curtain,  $c$  is the wave speed in the water column and  $c_b$  and  $k_b$  are the wave speed and wavenumber in the bubbly liquid.

$$A_+ = \frac{\exp(iks)}{\cos(k_b s) + (i/2)(c/c_b + c_b/c) \sin(k_b s)} \quad (4.4)$$

$$T = |A_+|^2 \quad (4.5)$$

This equation is modified, such that the width of the bubble curtain ( $s$ ) is depth dependent (4.6).

$$s(z) = \frac{s_{min} - s_{max}}{z_{max}} z + s_{max} \quad (4.6)$$

It is assumed that the width of the bubble curtain decreases in a linear way with depth (fig 4.6). Figure 4.3 shows the build up of the coefficient matrices. Figure 4.3a shows the frequency dependence. Here, the low frequencies are transmitted and the higher frequencies are damped. Figure 4.3b shows the transmission, but varying with depth. This means that near the seafloor there is more transmission than near the sea surface. By configuring the bubble curtain through  $s_{min}$  and  $s_{max}$  and comparing it to the measurement data, a coefficient matrix is iteratively constructed. It is assumed that the wave speed in the bubble curtain is constant with depth.

### 4.3 Depth-dependent wavenumber

To derive the depth-dependent wavenumber, the work of Bohne, Griebmann, and Raimund Rolfes (2019) is used and verified. Figure 4.4 shows three regions in a bubble curtain. In region I, which is near the nozzle, the bubbles form and rise due to buoyancy and momentum. The flows of nozzles merge in this stage. In region II a Gaussian flow profile is assumed. Region III contains horizontal flows induced by a return flow. Bohne, Griebmann, and Raimund Rolfes (2019) assumed that region II was extended over the entire depth thus neglecting region I and III.

The equation to be solved in this work is equation 4.7.

$$k_{eff}(\omega, x, z)^2 = \frac{\omega^2}{c_w^2} + 4\pi\omega^2 \int_0^\infty \frac{an(x, z, a)}{\omega_0(z, a)^2 - \omega^2 + 2ib(z, a)\omega} da \quad (4.7)$$

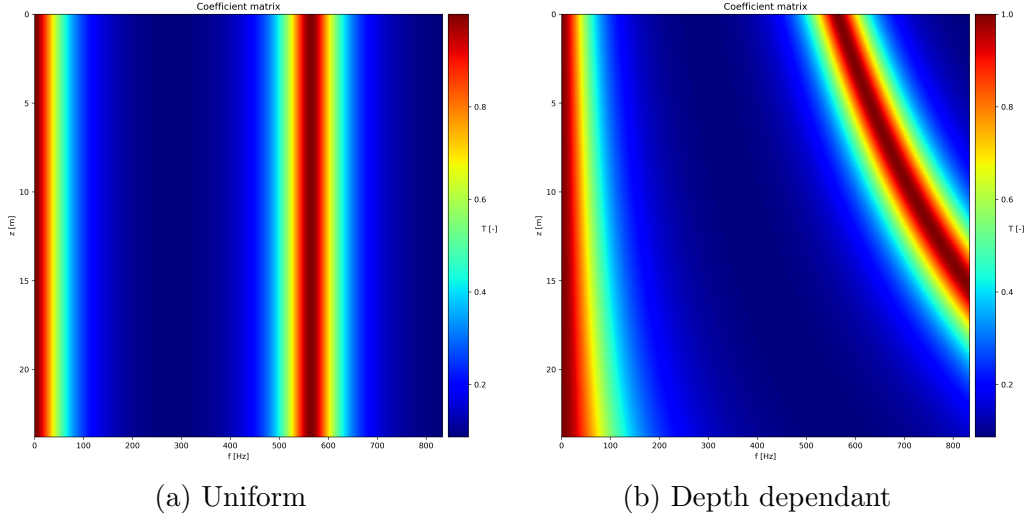


Figure 4.3: Coefficient Matrices. Red = 100% Transmission, Blue = 0% Transmission

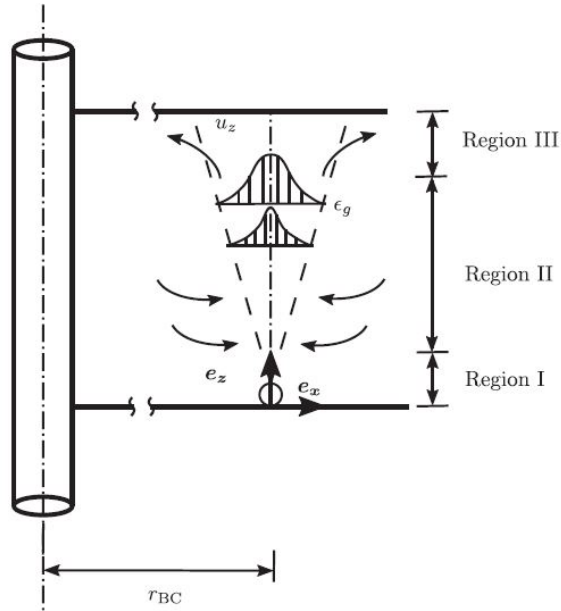


Figure 4.4: Description from the model (Bohne, Griebmann, and Raimund Rolfe, 2019)

Here,  $n(a, x, z)$  is calculated as follows with  $a$  being the bubble radius:

$$n(x, z, a) = f(a, x, z)N(x, z) \quad (4.8)$$

With  $f(a, x, z)$  being the Probability Density Function (PDF) of the bubble size.  $N(x, z)$ , the total number of bubbles, is calculated as follows:

$$N(x, z) = \frac{\epsilon(x, z)}{\bar{v}(x, z)} \quad (4.9)$$

Here,  $\epsilon_g$  is the local air fraction and  $\bar{v}$  is the mean bubble volume calculated as:

$$\bar{v}(x, z) = \int_0^\infty \frac{4}{3}a^3 f(a, x, z) da \quad (4.10)$$

First the PDF  $f(x, \mu, \sigma)$  is calculated according to the following equation.

$$f(a, \mu, \sigma) = \frac{1}{a\sigma\sqrt{2\pi}} \exp(-(\ln(a) - \mu^2)/2\sigma^2) \quad (4.11)$$

For validation purposes of the work by Bohne, Griebmann, and Raimund Rolfes (2019) the expected value  $\mu$  and standard deviation  $\sigma$  are taken as -6.70 and 0.67 respectively. These values were recommended in their work.

To calculate equation 4.9, the volume fraction  $\epsilon_g(x, z)$  are determined. This depends on the fluid dynamics within the bubble curtain. Bohne, Griebmann, and Raimund Rolfes (2019) present a simplified representation of the bubbly flow based on the momentum balance and continuity equations. They state the following set of equations that depend on the volume fraction  $\epsilon_g$  and bubble velocity  $\bar{u}_{lz}$ .

$$\frac{d}{dz} \int_{-\infty}^{\infty} (1 - \epsilon_g) \gamma \rho_l \bar{u}_{lz}^2 dx = \int_{-\infty}^{\infty} \epsilon_g \rho_l g dx \quad (4.12)$$

$$\frac{d}{dz} \int_{-\infty}^{\infty} (1 - \epsilon_g) \rho_l \bar{u}_{lz} dx = 2\alpha \rho_l u_{lzm} dx \quad (4.13)$$

As mentioned, the volume fraction and bubble velocity are assumed to have a Gaussian profile describing them as follows.

$$\bar{u}_{lz}(u_{lzm}, b, x) = u_{lzm} \exp(-x^2/b^2) \quad (4.14)$$

$$\epsilon_g(\epsilon_{gm}, b, x) = \epsilon_{gm} \exp(-x^2/(\lambda b)^2) \quad (4.15)$$

When substituted in equation 4.12 and 4.13 a standard solution is found. The solution comes in the following form:

$$\int_{-\infty}^{\infty} \exp(-x^2/a) dx = \sqrt{\frac{\pi}{a}} \quad (4.16)$$

Then equations 4.14 and 4.15 can be solved for the  $\epsilon_{gm}$  and  $u_{lzm}$ . The dependence on  $z$  comes from the half width  $b$  which can be readily solved as:

$$b(z) = \frac{\dot{m}_0}{\epsilon_{gm} \sqrt{\pi} \lambda \rho_g(z) \left( \frac{u_{lzm}}{\sqrt{\lambda^2 + 1 + u_{rel}}} \right)} \quad (4.17)$$

The density that varies over the depth is calculated with the ideal gas law, assuming an isothermal expansion of the bubble. This is derived in equation 4.18 through 4.20. Note that the mass is equal at the seafloor compared to the sea surface, by the law of conservation of mass.

$$P_0 V_0 = P_n V_n \quad (4.18)$$

$$P_0 \rho_{g0} \mathcal{M} = \rho_l g z \rho_g(z) \mathcal{M} \quad (4.19)$$

$$\rho_g(z) = \frac{\rho_{g0}}{P_0} (\rho_l g z + P_0) \quad (4.20)$$

$$(4.21)$$

Equations 4.12 and 4.13 are summarized in vector form.

$$\frac{d}{dz}(\mathbf{m}(\mathbf{u}, z)) = \mathbf{b}(\mathbf{u}, z) \quad (4.22)$$

Here,  $\mathbf{m}(\mathbf{u}, z)$  is the vector that contains the fluxes, the source terms are represented in vector  $\mathbf{b}$ . The unknowns  $\epsilon_{gm}$  and  $u_{lzm}$  are represented in the vector  $\mathbf{u} = [u_{lzm}, \epsilon_{gm}]^T$ . To derive the derivative of  $\mathbf{u}$  to  $z$ , the chain rule is applied resulting in the following.

$$\frac{\partial \mathbf{m}}{\partial \mathbf{u}} \frac{d\mathbf{u}}{dz} = \mathbf{b} - \frac{\partial \mathbf{m}}{\partial z} \quad (4.23)$$

By left multiplying with the inverse of  $\frac{\partial \mathbf{m}}{\partial \mathbf{u}}$  the derivative of  $\mathbf{u}$  with respect to  $z$  is calculated in the following manner.

$$\left(\frac{\partial \mathbf{m}}{\partial \mathbf{u}}\right)^{-1} \frac{\partial \mathbf{m}}{\partial \mathbf{u}} \frac{d\mathbf{u}}{dz} = \left(\frac{\partial \mathbf{m}}{\partial \mathbf{u}}\right)^{-1} \left(\mathbf{b} - \frac{\partial \mathbf{m}}{\partial z}\right) \quad (4.24)$$

$$\frac{d\mathbf{u}}{dz} = \left(\frac{\partial \mathbf{m}}{\partial \mathbf{u}}\right)^{-1} \left(\mathbf{b} - \frac{\partial \mathbf{m}}{\partial z}\right) \quad (4.25)$$

This first-order ordinary differential equation is solved with a Forward Euler iteration.

$$\mathbf{u}_{n+1} = \mathbf{u}_n + \frac{d\mathbf{u}_n}{dz} \Delta z \quad (4.26)$$

### Initial conditions

The derivation of the initial conditions depends on both the half width  $b$  and the initial centerline velocity  $u_{lzm}$ . They cannot be calculated explicitly so an iteration approach is used. The initial volume fraction ( $\epsilon_{gm0}$ ) is set to 0.95 which is recommended by Bohne, Griebmann, and Raimund Rolfes (2019).

$$b_0(z) = \frac{\dot{m}_0}{\epsilon_{gm0} \sqrt{\pi} \lambda \rho_{g0}(z) \left(\frac{u_{lzm0}}{\sqrt{\lambda^2 + 1 + u_{rel}}}\right)} \quad (4.27)$$

$$u_{lzm0} = \frac{\sqrt{2} \sqrt{M_0} (2\lambda^2 + 1)^{(1/4)}}{\pi^{(1/4)} \sqrt{(\sqrt{4\lambda^2 + 2} - 2\epsilon_{gm0}\lambda)\gamma b_0(z)\rho_l}} \quad (4.28)$$

For a stable iteration a  $\Delta z$  of 0.0001 was advised. Other parameters that are used are summarized below. These values are based on the work of Bohne, Griebmann, and Raimund Rolfes (2019).

The initial momentum flux  $M_0$ , used in equation 4.28, is defined as follows:

$$M_0 = \frac{4\Delta y_n \dot{m}_0^2}{\pi \rho_{g0} d_n^2} \quad (4.29)$$

The figure below shows the obtained result compared to the work of Bohne, Griebmann, and Raimund Rolfes (2019). This is done for the same air flows used

Quantity	Variable	Value	Unit
Spreading coefficient	$\lambda$	0.2	-
Amplification factor	$\gamma$	1.0	-
Entrainment coefficient	$\alpha$	0.16	-
Relative velocity	$u_{rel}$	0.4	m/s
Airflow	$\dot{m}_0$	0.003	m <sup>2</sup> /s
Nozzle spacing	$\Delta y_n$	0.1	m

Table 4.1: Unknown parameters (Bohne, Griebmann, and Raimund Rolfes, 2019)

in this work. It stands out that the trend of the solutions is the same. However, because the same initial conditions are not found, a slight deviation is observed. Nevertheless, a stable solution is observed which also shows the sensitivity on the initial conditions.

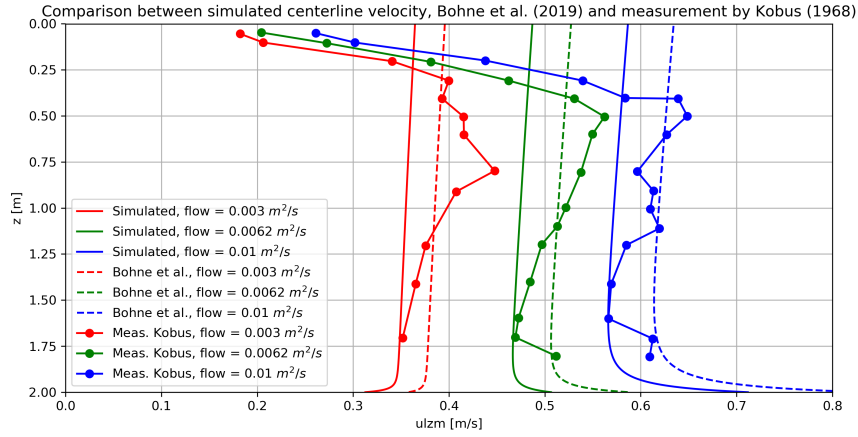


Figure 4.5: Comparison of the centerline velocity between simulation and original work (Bohne, Griebmann, and Raimund Rolfes, 2019) and measurements (Kobus, 1968)

It is important to note that this extension is analyzed to see whether this method could be applied to SILENCE. However, this depth dependant wavenumber approach is not used in scenario 3 of the bubble curtain study (sec. 4.4) because the complexity of solving (4.7) does not add to the scope of this research. Nevertheless, it could be a viable method to model a bubble curtain based on airflow, nozzle diameter and nozzle spacing because it gives more physical sense to the input parameters that are used in reality.

## 4.4 Bubble curtain scenario's

To analyze the noise reduction level by a BBC, three scenarios are considered (figure 4.6). Scenario 1 is the modeling of a perfect BBC, which blocks an entire waterborne path. This is done by generating noise at a desired distance ( $r_{bc}$ ). The output from the SILENCE Near-field module that runs in the soil is fed in the propagation module, thus neglecting the waterborne path. By doing this, the maximum achievable noise reduction can be assessed. Additionally, this provides insight in the contribution of the soil to the underwater noise.

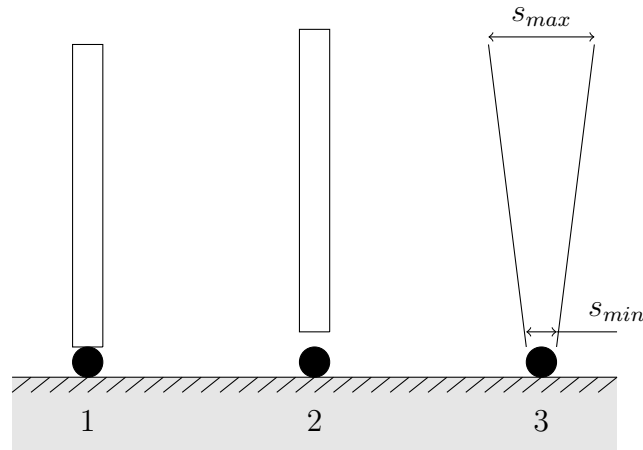


Figure 4.6: Schematic representations of Bubble curtain configurations, 1. Full block, 2. Partial block, 3. Artificial BBC

The next case consists of a full block of the water column, except there is a 1m gap created that lets sound pass through. This is done to mimic the reduced effectiveness of the BBC near the seabed. With this setup, the noise contribution of this gap is examined.

The final case is to artificially implement a BBC. This is done by reducing the output of the SILENCE Near-field module and feeding it in the propagation module. The damping of a BBC is done by decreasing the pressure values based on frequency and depth. The z-dependancy is done to account for the varying thickness of the bubble curtain along the z-axis. Note that physical properties of a BBC such as volume fraction, varying density and varying wave speeds are neglected. This method is explained in depth in section 4.2.

For each of the cases mentioned in figure 4.6, a parametric study is conducted to investigate the influence of the bubble curtain radius ( $r_{bc}$ ) is on the transmission of noise. This study is presented in section 5.

## 4.5 Bubble curtain validation results

To validate the effective source reduction model, a comparison was made with the data obtained at the █████ OWF. First, the sound exposure level (SEL), and peak pressure ( $L_{p,pk}$ ) were compared (fig. 4.7). Additionally, the result from the simulations was compared in frequency domain to see the reduction per frequency bin (fig. 4.8). This was compared with the work of Elzinga et al. (2019).

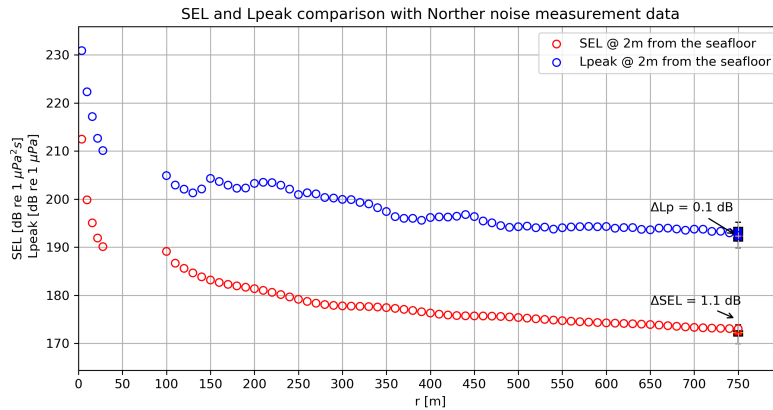


Figure 4.7: Comparison between the SEL and  $L_{p,pk}$  of the measurement data and the simulation with the bubble curtain. Note that the internationally standard symbol for peak pressure ( $L_{p,pk}$ ) is denoted as  $L_{peak}$  in the figure.

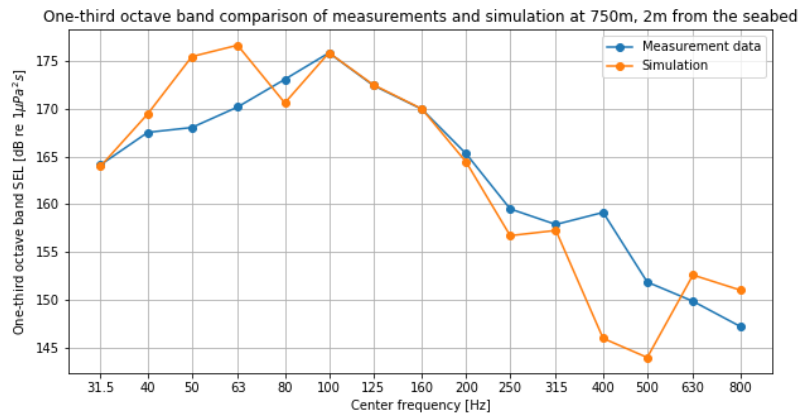


Figure 4.8: Comparison of noise reduction in one-third octave bands

This was iteratively found by adjusting the lower ( $s_{min}$ ) and upper ( $s_{max}$ ) width of the bubble curtain. In this case  $s_{min} = 0.1\text{m}$  and  $s_{max} = 0.2\text{m}$  had noise values which are in good agreement with the measurement data. Note that this approach is a forward approach. For future applications it is desired model in a predictive way. Therefore, a sensitivity analysis is shown in appendix C. It is visible that changing the lower width is more sensitive to the noise reduction compared to the upper width.

# Chapter 5

## The location of the bubble curtain

In this section the location of the bubble curtain is examined by means of a parametric study, the methodology is presented in section 5.1. Followed by the results and discussion presented in section 5.2 and 5.4 respectively. Finally, some flaws and improvements of the model are discussed.

### 5.1 Methodology of the parametric study

The parametric study of the bubble curtain is conducted for the three cases mentioned in section 4.4. The placement of the bubble curtain at  $r_{bc}$  is done by generating a near field prognosis with the SILENCE generation module up to  $r_{bc}$ , next the effective source reduction method is applied and finally the SILENCE propagation model propagates the reduced noise field up to 750m with an input coordinate of  $(r_{bc}, z_0)$ .

With the time domain solution at 750m, the sound exposure level and peak pressure level are calculated according to (2.8) and (2.5) respectively. This procedure is performed for different bubble curtain locations ( $r_{bc}$ ) in a range from 10m up to 150m from the pile wall. The noise reduction can be calculated by comparing the noise from the mitigated case to the free-field case as shown in (5.1) and (5.2).

$$\Delta SEL = SEL_{ref} - SEL_c \quad (5.1)$$

$$\Delta L_{p,pk} = L_{p,pk,ref} - L_{p,pk,c} \quad (5.2)$$

Here, the reference case was the unmitigated simulation. The subscript  $c$  denotes the mitigation case type (fig. 4.4) that was applied.

### 5.2 Result of the parametric study

In this section, the result of this study is presented. Figure 5.1 shows the SEL and  $L_{p,pk}$  reduction of the aforementioned bubble curtain cases (section 4.4). The graphs per case are presented in appendix B.

By taking a look at appendix B, a clear trend is visible for every case. It shows that the noise reduction increases when the bubble curtain is placed further away from the pile. However, there is a tipping point where a plateau is reached where the

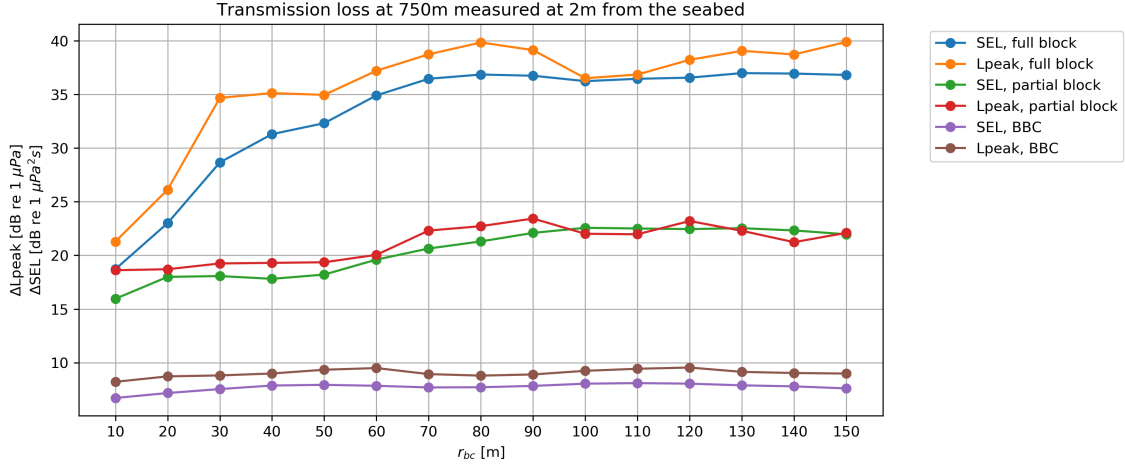


Figure 5.1:  $\Delta SEL$  and  $\Delta L_{p,pk}$  for a bubble curtain placed at different ranges from the piles surface.

bubble curtain radius does not influence the noise reduction anymore. This tipping point can be an ideal location for a bubble curtain.

When comparing the partial block and BBC case with the full block case as shown in figure 5.1, it is visible that the trend flattens out for the partial block and BBC case. In other words. The worse the noise reduction mechanism, the smaller the difference between the minimum noise reduction and the noise reduction at the tipping point. This is summarized in table 5.1. The location of the tipping point differs per case. There is no clear trend visible for this matter. Nevertheless it is expected that the noise reduction for a bubble curtain near the pile does influence the noise reduction since other effects come into play such as destructive or constructive interference and the longest wavelength might not be fully blocked.

Case:	Min reduction [dB]:	Reduction at tipping point [dB]:	$\Delta SEL$ [dB]:	Tipping point [m]
1.	18.7	37	18.3	70
2.	16	22.6	6.6	90
3.	6.7	8.1	1.3	50

Table 5.1: Difference between minimum and maximum noise reduction for different cases

### 5.3 Relation of the tipping point to the energy leakage

In this section, the possible causes of the effective bubble curtain location are discussed. As mentioned before (Figure 4.2), two possible energy leakage phenomena are expected namely the upward moving Mach cone and leakage due to tunneling.

By looking at the upward moving Mach cone, an approximation can be made of the distance where the Mach cone ultimately penetrates the water column. Note that different soil layers, refract and reflect this compressive wave. However, it is

not expected that refraction has a large influence on the maximum distance. On the contrary, the reflection between soil layer may have an effect. Especially for the part of the Mach wave that travels the longest path to the water column (radiated from the pile tip). One could argue whether this wave front makes it to the water column thus in reality the effect of the upward Mach cone has more effect close to the pile.

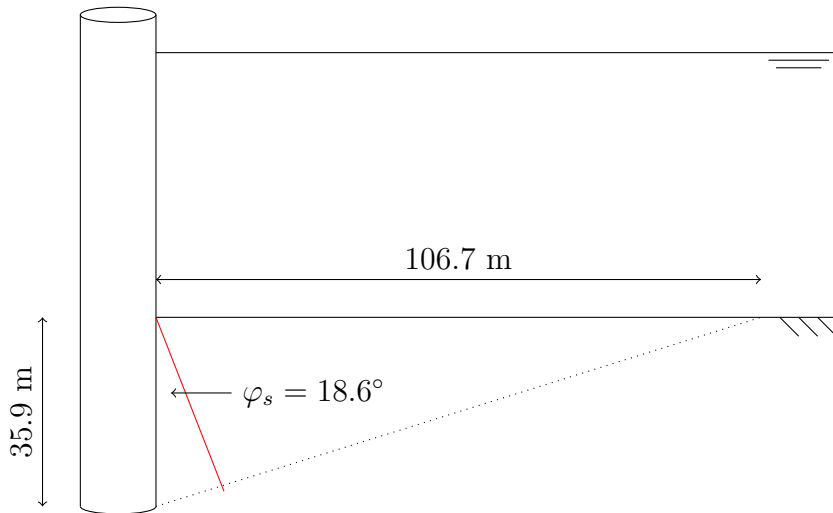


Figure 5.2: Rough approximation of the maximum horizontal distance over which the upward moving Mach cone can penetrate the water column.

By taking the energy leakage into account as a whole, like shown in figure 5.3, it is visible that energy radiation is present and decays over distance from the pile. The energy radiation is still effective up to 70m, this can be derived from the tipping point of the full block case. However, it is not clear if either the tunneling effect or the Mach cone is responsible for this effect. The ultimate mechanism contributing to the noise leakage back to the water column will also depend on the stratigraphy of the soil layers below.

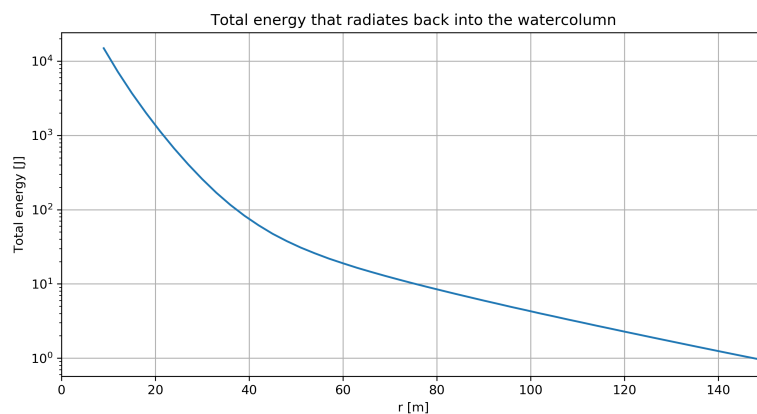


Figure 5.3: Total energy that radiates back in the water column for the free field case

Ultimately, the distance of the tipping point is influenced by the energy leakage in

the water column. This energy leakage is a combination of an upward traveling Mach cone and the tunneling effect. The contribution of each phenomenon to the energy leakage is not observed. It is arguable which contribution of these phenomena is dominant in certain cases. Figure 3.19 shows that the energy leakage is proportional to the force amplitude. The contribution of the soil is not examined.

## 5.4 Trend of the noise reduction potential

Figure 5.1 shows that the bubble curtain radius has less influence on the noise reduction when more noise is let through the bubble curtain case i.e. from full block to bubble curtain. This trend, together with the validation of the bubble curtain model (figure 4.7 and 4.8), indicates that the bubble curtain location has minor influence on the noise reduction and can therefore be placed closer to the pile. It is recommended to verify this based on experiments.

## 5.5 Model flaws

The result which is discussed can be influenced by assumptions in the model. This model does not include reflection of the bubble curtain nor the scattering of the noise field. This scattering has influence on the transmission characteristics. In this model the amplitude is reduced based on the frequency content and depth. This model could be improved by modifying the particle velocity vectors based on the bubble curtain characteristics to examine whether the scattering has an effect to the noise reduction trend.

# Chapter 6

## Conclusion and recommendations

The growing demand for renewable energy triggered the development of larger offshore wind turbines, resulting in larger foundations to place them on, deeper waters and less favorable soil. Underwater noise that results from pile driving can do serious harm to aquatic life. Currently with all mitigation measures, installation still reaches the legal limits. Bubble curtains are deployed to reduce noise emissions from offshore piledriving. This research aims to identify the critical parameters that can influence the location of the bubble curtain. In this chapter the results of this research are discussed and concluded, finally a recommendation is given.

### 6.1 Discussion and concluding remarks

This scope of this research was to identify the critical parameters that determine the optimal position of a bubble curtain. For this purpose, the SILENCE model (Tsouvalas, 2015) was used to analyze the physical effects that occur in the water column and soil as a result of a hammer blow.

First, a literature study was performed with the purpose of gaining an understanding on ocean acoustics. This literature study also gave insight in the existing models that are related to noise generation during pile driving. It is worth mentioning that the state of the art models are able to capture the physical effects that occur in both the water column and soil. This means that the effects of shear waves and Scholte waves are included. SILENCE, the model used in this research, belongs to the second generation of models. The SILENCE model uses a semi-analytical approach which comes with the benefit of computational efficiency. In previous studies (Tsouvalas, 2015) it was able to predict noise within  $\pm 2$ dB accuracy.

Prior to working with SILENCE, a validation study was performed which brings us to the first sub-question of this research. What is the accuracy of SILENCE compared to the measurement data? Here, the accuracy and validity of SILENCE were examined. This was done by comparing the noise simulation to the measurement data, obtained at a few unmitigated installations at the █████ OWF. The comparison of the sound exposure level and peak pressure level at 750m gave similar results. The peak pressure was simulated with 2.2 dB deviation from the mean and the sound exposure level was simulated with a 1.7 dB from the mean. Time domain plots showed physical arrival times of the wave-fronts and the simulated frequency spectrum had a similar trend as the median frequency spectrum from the measurements. These results were in agreement with previous studies (Tsouvalas, 2015).

Therefore, validity of SILENCE is proven.

After conducting the validation study, the implementation of a bubble curtain was studied to answer the following question. How can a bubble curtain be implemented in the SILENCE software? The basic idea was to generate a source in the SILENCE generation module, artificially dampen this source and use this dampened source in the propagation module to calculate the noise levels at larger distances. This is also referred to as an effective source reduction. To dampen the source, the output of the generation module was multiplied with a coefficient matrix with a unique damping value per frequency and depth. The coefficients were based on the work of Bohne, Griesmann, and Raimund Rolfes (2019). The transmission coefficient, as described in (4.5), was slightly modified to account for the varying width of the bubble curtain over depth. The input for the bubble curtain model was defined as the minimum and maximum width of the bubble curtain. Based on that input, a configuration was iteratively found. The validity of this method was tested by comparing it to the bubble screen installations from the ████████ OWF dataset. Here, the frequency spectrum and the SEL and  $L_{p,pk}$  were compared. The frequency spectrum had the same trend as the measurements. The SEL and  $L_{p,pk}$  deviated 1.1 dB and 0.1 dB from the mean of the measurements respectively. Therefore, the validity of this method was demonstrated. However, this method includes only the transmission characteristics of a bubble curtain, whereas reflection is neglected. Therefore, noise levels before the bubble curtain lack reflected waves. Nevertheless, this did not influence this study since it focused on the noise reduction of the field outside the bubble curtain. Scattering of the incoming noise field was also neglected. This could influence the noise transmission.

The last sub-question to answer is why to place a bubble curtain in a certain manner. This is analyzed in two ways. First the energy flux and frequency spectra were analyzed at the seafloor. This showed that energy leakage from soil to water is present over a radial range between 10 to 150m from the pile wall. The frequency content is mainly shifted towards low frequencies. Next, a parametric study was performed for three bubble curtain configurations. The three cases were a "perfect" bubble curtain, a "perfect" bubble curtain with a 1m gap at the bottom and a realistic approach mentioned in the previous paragraph. For these three cases, a bubble curtain radius was applied between 10m and 150m with steps of 10m. All three cases show less noise reduction if the BBC is placed in the vicinity of the pile. The minimum radii are summarized in table 6.1.

Case:	Minimum $r_{bc}$ [m]	Reduction potential [dB re 1 $\mu Pa$ ]
Full block	70m	18.3
Partial block	90m	6.6
Bubble curtain	40m	1.3

Table 6.1: Minimum radius per case and reduction potential

However, the results also show a trend that when more noise is transmitted in comparison to a full-block, the noise reduction potential becomes less when the bubble curtain is placed further away from the pile. The noise leakage plays a key role in this. However, other effects like the longest wavelength and destructive or constructive interference also play a role. When a full-block is placed "too far" away a plateau in noise reduction is reached. It is the tipping point where the optimal

position of a bubble curtain could be. However, if the transmission characteristics of a bubble curtain are modelled based on frequency content the effect of the bubble curtain radius on the noise reduction potential becomes much less influential. For example, placing the full block further away from the pile (up to 70m) can lead to a noise reduction of 18 dB, for the bubble curtain case this potential is only 1.6 dB. This is because the frequency content of the leakage is mainly shifted towards low frequencies ( $\sim 31.5$  Hz). A bubble curtain is not very effective in this frequency range.

Finally, the main goal of this research was to find the critical parameters that determine the location of the bubble curtain. It can be concluded from this research is that the distance of the bubble curtain matters and that the energy leakage from the soil in the water column contributes to that location. Figure 3.16, 3.17 and 5.1 confirm this. It is not

## 6.2 Recommendations

In this section, the recommendations of this research are presented. First, suggestions are given in order to get a better understanding of the effects in the soil on the location of a bubble curtain. Next, the bubble curtain implementation is discussed and how to improve it. Finally, a recommendation on the SILENCE model is presented.

This research shows that the bubble curtain position matters for the effectiveness of the noise reduction. For a full block of the waterborne path, the most effective location was at 70m. However, the difference in soil type was not examined. To gain a further understanding of the relation between soil parameters and energy leakage, it is recommended to do a parametric study with different soil parameters. To do this, multiple simulations need to be performed and for that reason a source needs to be generated at a close distance from the pile which benefits the computational time. Then the SILENCE propagation module should be used to calculate the response at larger distances.

It was also visible that the noise reduction potential for a bubble curtain case was lower than for a full block. This is because the energy leakage is mainly shifted towards low frequencies at which a bubble curtain is not effective. Therefore, one could argue whether the location of a bubble curtain matters. It is recommended to verify this by experiments. Additionally, this low frequency leakage can be mitigated by near field noise mitigation systems such as AdBm and HSD. The effectiveness of these systems can be argued because significant leakage happens up to 100 m. It is possible that the frequencies for which these systems are "tuned" propagate underneath the near field system. It is recommended to see whether such systems can be improved by deploying them at larger distances.

To mimic the transmission characteristics of a bubble curtain, an effective source reduction model was built. This approach gave valid results in comparison to the measurement data (Van Oord, 2018). The shape of the bubble curtain was determined iteratively. This means that the lower and upper width of the bubble curtain were configured until a match with the measurement data (Van Oord, 2018) was found. This method was a forward approach. It is desired to have a more predictive approach in the future. In this work, the transmission characteristics were derived under the assumption that the wave speed is constant in the bubbly medium.

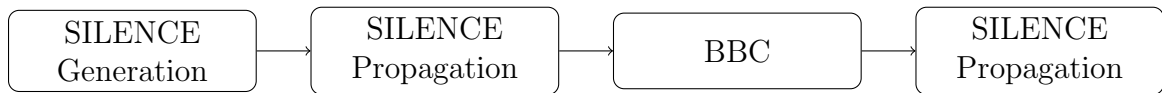


Figure 6.1: Recommended approach for use of the effective source reduction

Bohne, Griebmann, and Raimund Rolfes (2019) proposed to calculate the transmission characteristics based on bubble size distributions. Even though this method was verified, it was not used in this research. To gain a better understanding of the relation between the noise reduction and the input parameters of a bubble curtain (airflow, nozzle spacing and nozzle diameter), this method by Bohne, Griebmann, and Raimund Rolfes (2019) can be an effective way to improve to the effective source reduction approach. Additionally, scattering of the waves was also not included. It is expected that scattering might have an influence on the noise data recorded at 750m. It is also recommended to further examine this.

The effective source reduction showed its validity but using this approach at larger distances required more computational effort since a deep rigid boundary was applied in the simulations. The application of a deep rigid boundary condition frustrated the efficiency of the model and was not necessary. However, in this research the bubble curtain model was applied to the output of the SILENCE generation module. For future research it is recommended to generate a noise field in the SILENCE generation module with a shallow rigid boundary condition. The next step would be to propagate this field with the propagation module. This output should then be reduced by the effective source reduction method and finally be propagated to larger distances (Figure 6.1). The effective source reduction mechanism is programmed generically in a python toolbox which is presented in appendix D. It can therefore be adopted for future research.

Lastly, the application of SILENCE is discussed here. If we look to the state of the art models, SILENCE belongs to the second generation of models that describe the noise related to offshore piledriving. With second generation is meant that soil effects are included in the model opposed to first generation models where the soil was modelled as an equivalent fluid. By taking the soil into account, shear waves and Scholte waves become visible which contributes to a more complete understanding of the different contributions to underwater noise. SILENCE uses a semi-analytical approach. This approach requires less computational effort than full FE. Furthermore, SILENCE was able to predict underwater noise with a  $\pm 2$  dB accuracy. For these reasons, SILENCE is suitable for doing many calculations in a short time albeit under the right modeling assumptions. Therefore, SILENCE is a useful method to study the physical aspects of underwater noise in a thorough manner.

However, SILENCE requires specialist knowledge to be used effectively. Working with SILENCE is not yet 'user friendly' and takes time to understand how simulations should be performed and why some simulations 'crash'. For that reason, it is recommended to add an error report or manual to the software. This way, reasons for errors can be found more easily.

# Bibliography

- Aziman, M et al. (2016). “Compressive and Shear Wave Velocity Profiles using Seismic Refraction Technique”. In: *Journal of Physics: Conference Series* 710, p. 012011. DOI: 10.1088/1742-6596/710/1/012011.
- Bellmann, Michael A., ed. (2018). *Noise mitigation during large foundations*. Institut für technische un angewandte physik GMBH, Germany.
- Bellmann, Michael A. (2019). *Measurements of the underwater noise during the installation of the OSS and OWTG foundations in the Offshore Windfarm* [REDACTED]. Tech. rep. Institut für technische un angewandte physik GmbH.
- Bohne, Tobias, Tanja Griebmann, and Raimund Rolfes (2019). “Modeling the noise mitigation of a bubble curtain”. In: *The Journal of the Acoustical Society of America* 146.4, pp. 2212–2223. DOI: 10.1121/1.5126698.
- Britannica, Encyclopædia (2020). URL: <https://www.britannica.com/science/seismograph/Applications-of-the-seismograph#/media/1/532943/210259>.
- Chapman, David and Dale Ellis (June 1998). “The elusive decibel: Thoughts on sonars and marine mammals”. In: *Canadian Acoustics / Acoustique Canadienne* 26, pp. 29–31.
- Commander, Kerry W. and Andrea Prosperetti (1989). “Linear pressure waves in bubbly liquids: Comparison between theory and experiments”. In: *The Journal of the Acoustical Society of America* 85.2, pp. 732–746. DOI: 10.1121/1.397599.
- Diederichs, Ansgar et al. (Mar. 2014). *Entwicklung und Erprobung des Großen Blasenschleiers zur Minderung der Hydroschallemissionen bei Offshore-Rammarbeiten. Schlussbericht*. Tech. rep.
- Elmer, Karl-Heinz and John R. Savery, eds. (2014). *New Hydro Sound Dampers to reduce piling underwater noise*. Offnoise-Solutions GmbH. INTER-NOISE, NOISE-CON Congress 927, and Conference Proceedings.
- Elzinga, Jesper et al. (2019). *Installing Offshore Wind Turbine Foundations Quieter: A Performance Overview of the First Full-Scale Demonstration of the AdBm Underwater Noise Abatement System*. Tech. rep. van Oord.
- Froeze, Michelle (2019). *AdBm noise-mitigation system successfully tested for offshore wind*. <https://www.windpowerengineering.com/adbm-noise-mitigation-system-successfully-tested-for-offshore-wind/>.

- Glorieux, Christ et al. (2001). “On the character of acoustic waves at the interface between hard and soft solids and liquids”. In: *The Journal of the Acoustical Society of America* 110.3, pp. 1299–1306. DOI: 10.1121/1.1396333. eprint: <https://doi.org/10.1121/1.1396333>. URL: <https://doi.org/10.1121/1.1396333>.
- Göttsche, Klaus (Sept. 2013). “Numerical prediction of underwater noise reduction during offshore pile driving by a Small Bubble Curtain”. In:
- Hou, Zhengyu et al. (2018). “Acoustic impedance properties of seafloor sediments off the coast of Southeastern Hainan, South China Sea”. In: *Journal of Asian Earth Sciences* 154, pp. 1–7. ISSN: 1367-9120. DOI: <https://doi.org/10.1016/j.jseaes.2017.12.003>. URL: <http://www.sciencedirect.com/science/article/pii/S1367912017306788>.
- Jensen, Finn B. et al. (2011). *Computational ocean acoustics*. second. Springer.
- Kaplunov, J. D, L. Yu Kossovitch, and E. V Nolde (1998). *Dynamics of Thin Walled Elastic Bodies*. Elsevier Science.
- Kobus, Helmut E. (Jan. 1968). “Analysis of the flow induced by air bubble systems”. In: *Coastal Engineering Proceedings* 1.11, p. 65. DOI: 10.9753/icce.v11.65. URL: <https://icce-ojs-tamu.tdl.org/icce/index.php/icce/article/view/2568>.
- Kuhn, Christian et al. (2014). *Dynamic measurements of pile deflections as a source of underwater sound emissions during impact driving of offshore pile foundations*. Tech. rep. Technische Universität Braunschweig, Institute for Soil Mechanics and Foundation Engineering, Germany.
- Lefebvre, J.P. (1999). “Chapter 1 - Physical Basis of Acoustics”. In: *Acoustics*. Ed. by Paul Filippi et al. London: Academic Press, pp. 1–39. ISBN: 978-0-12-256190-0. DOI: <https://doi.org/10.1016/B978-012256190-0/50002-6>. URL: <http://www.sciencedirect.com/science/article/pii/B9780122561900500026>.
- Lippert, Marco Huisman, et al. (2017). “Prognosis of underwater pile driving noise for submerged skirt piles of jacket structures”. In: *UACE2017 - 4th Underwater Acoustics Conference and Exhibition*.
- Lippert and Lippert (Dec. 2012). “Modelling of pile driving noise by means of wavenumber integration”. In: *Acoustics Australia / Australian Acoustical Society* 40, pp. 178–182.
- Lippert, Marten Nijhof, et al. (Apr. 2016). “COMPILE—A Generic Benchmark Case for Predictions of Marine Pile-Driving Noise”. In: *IEEE Journal of Oceanic Engineering*, pp. 1–11. DOI: 10.1109/JOE.2016.2524738.
- Lucke, Klaus et al. (Nov. 2011). “The use of an air bubble curtain to reduce the received sound levels for harbor porpoises (*Phocoena phocoena*)”. In: *The Journal of the Acoustical Society of America* 130, pp. 3406–12. DOI: 10.1121/1.3626123.
- Matuschek, Rainer and Klaus Betke (Jan. 2009). “Measurements of Construction Noise During Pile Driving of Offshore Research Platforms and Wind Farms”. In: *Proc. NAG/DAGA Int. Conference on Acoustics*.

- Meegan, G. D. et al. (1999). “Nonlinear Stoneley and Scholte waves”. In: *The Journal of the Acoustical Society of America* 106.4, pp. 1712–1723. DOI: 10.1121/1.427920. eprint: <https://doi.org/10.1121/1.427920>. URL: <https://doi.org/10.1121/1.427920>.
- Menck GmbH (2016). URL: <https://www.menck.com/pilesize/3500kj>.
- Minnaert, M. (1933). “XVI. On musical air-bubbles and the sounds of running water”. In: *The London, Edinburgh, and Dublin Philosophical Magazine and Journal of Science* 16.104, pp. 235–248. DOI: 10.1080/14786443309462277. eprint: <https://doi.org/10.1080/14786443309462277>. URL: <https://doi.org/10.1080/14786443309462277>.
- Müller, Andreas and Carsten Zerbs (2011). *Measuring instruction for underwater sound monitoring*. Bundesamt für Seeschifffahrt und Hydrographie.
- Peng, A. Tsouvalas, and A.V. Metrikine (Aug. 2019). “Underwater noise generated by offshore pile driving: A pile-soil-water vibro-acoustic model based on a mode matching method”. In: *Conference Proceedings of the 5th Underwater Acoustics Conference and exhibition 2019*.
- Peng, A. Tsouvalas, and A.V. Metrikine (2020). “A coupled modelling approach for the fast computation of underwater noise radiation from offshore pile driving”. In: EURO DYN 2020.
- Ramirez, Lizet et al. (2020). *Offshore wind in Europe, key trends and statistics*. Tech. rep. WindEurope.
- Reinhall, Per G. and Peter H. Dahl (2011). “Underwater Mach wave radiation from impact pile driving: Theory and observation”. In: *The Journal of the Acoustical Society of America* 130.3, pp. 1209–1216. DOI: 10.1121/1.3614540.
- Rijkswaterstaat (2016). URL: <https://wetten.overheid.nl/BWBR0037801/2016-04-09>.
- Rumes, B. et al. (2018). “Evaluating underwater noise regulations for piling noise in Belgium and The Netherlands”. In: *Environmental impacts of offshore wind farms in the Belgian part of the North Sea: Environmental impact monitoring*. Royal Belgian Institute of Natural Sciences et al. Chap. 4. ISBN: 978-9-0732-4242-5.
- Rustemeier, J., Tanja Griebmann, and R. Rolfes (Jan. 2012). “Underwater sound mitigation of bubble curtains with different bubble size distributions”. In: *Proceedings of Meetings on Acoustics* 17. DOI: 10.1121/1.4772936.
- Seidel, Dr. Ing. Marc (2014). “Substructures for offshore wind turbines. Current trends and developments”. In: *Festschrift Peter Schaumann*.
- Skopljak, Nadja (2019). *Van Oord and AdBm Test New Noise Mitigation System*. <https://www.offshorewind.biz/2019/05/02/van-oord-and-adbm-test-new-noise-mitigation-system/>.
- Thomsen, Kurt E. (2014a). “Chapter Eighteen - Environmental and Other Issues”. In: *Offshore Wind (Second Edition)*. Ed. by Kurt E. Thomsen. Second Edition.

- Boston: Academic Press, pp. 331–352. ISBN: 978-0-12-410422-8. DOI: <https://doi.org/10.1016/B978-0-12-410422-8.00018-2>. URL: <http://www.sciencedirect.com/science/article/pii/B9780124104228000182>.
- Thomsen, Kurt E. (2014b). “Chapter Eleven - Commonly Used Installation Methods”. In: *Offshore Wind (Second Edition)*. Ed. by Kurt E. Thomsen. Second Edition. Boston: Academic Press, pp. 177–202. ISBN: 978-0-12-410422-8. DOI: <https://doi.org/10.1016/B978-0-12-410422-8.00011-X>. URL: <http://www.sciencedirect.com/science/article/pii/B978012410422800011X>.
- Tsouvalas, A. (2015). “Underwater noise generated by offshore pile driving”. PhD thesis. TU Delft.
- Tsouvalas, A. (June 2020). “Underwater Noise Emission Due to Offshore Pile Installation: A Review”. In: *Energies* 13. DOI: 10.3390/en13123037.
- Tsouvalas, A. and A.V. Metrikine (2016). “Noise reduction by the application of an air-bubble curtain in offshore pile driving”. In: *Journal of Sound and Vibration* 371, pp. 150–170. ISSN: 0022-460X. DOI: <https://doi.org/10.1016/j.jsv.2016.02.025>. URL: <http://www.sciencedirect.com/science/article/pii/S0022460X16001681>.
- Van Oord (2016). *Constructing the Arkona offshore wind farm in the Baltic Sea*. <https://www.vanoord.com/activities/constructing-arkona-offshore-wind-farm-baltic-sea>.
- Van Oord (2018). Noise data from the ██████████ field, courtesy of Van Oord.
- Yilmaz, Öz and Richard D. Miller (2015). *Engineering Seismology with Applications to Geotechnical Engineering*. SEG (Society of Exploration Geophysicists). ISBN: 978-1-56080-329-4. URL: <https://app.knovel.com/hotlink/toc/id:kpESAGE003/engineering-seismology/engineering-seismology>.
- Zampolli, Mario et al. (2013). “Validation of finite element computations for the quantitative prediction of underwater noise from impact pile driving”. In: *The Journal of the Acoustical Society of America* 133.1, pp. 72–81. DOI: 10.1121/1.4768886.

## A Bathymetry

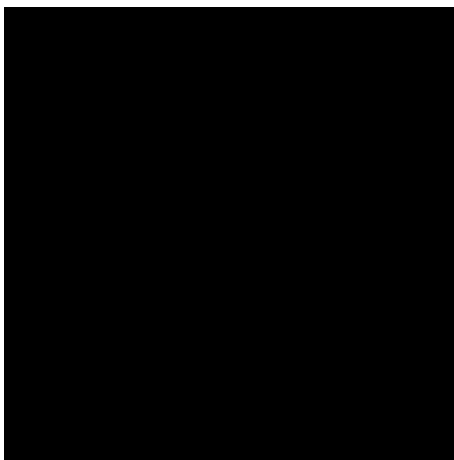
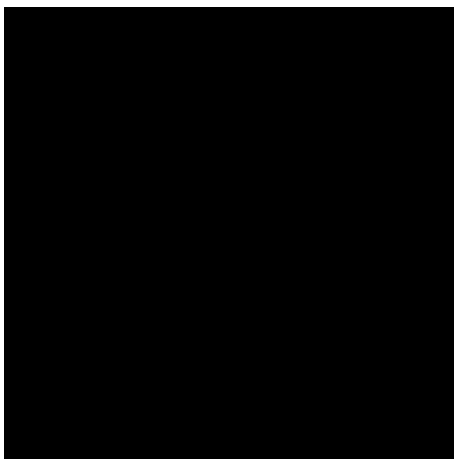
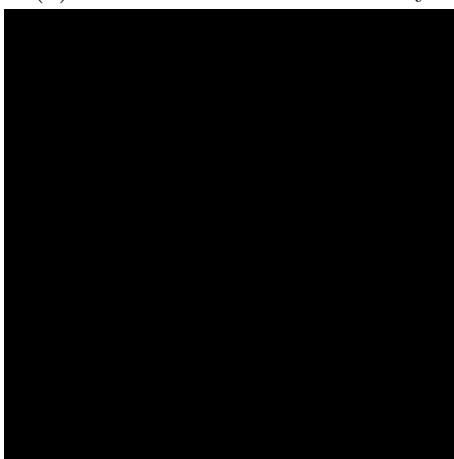


Figure A.2: Censored for confidentiality



(a) Censored for confidentiality



(b) Censored for confidentiality

Figure A.3: Censored for confidentiality

## B Zoom in of parametric study on bubble curtain location

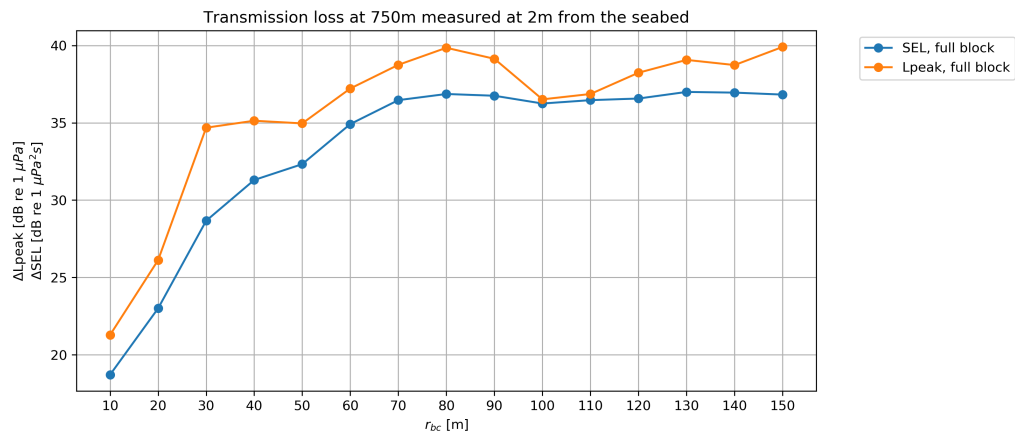


Figure B.4: Full block

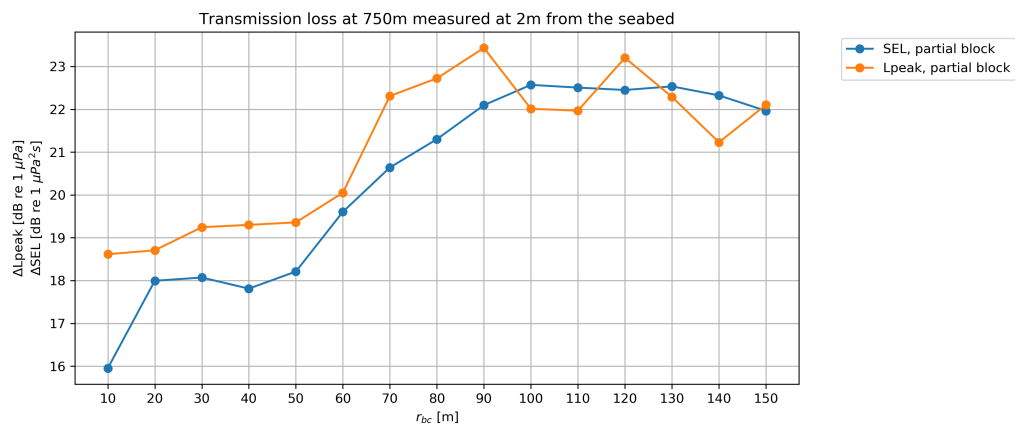


Figure B.5: Partial block

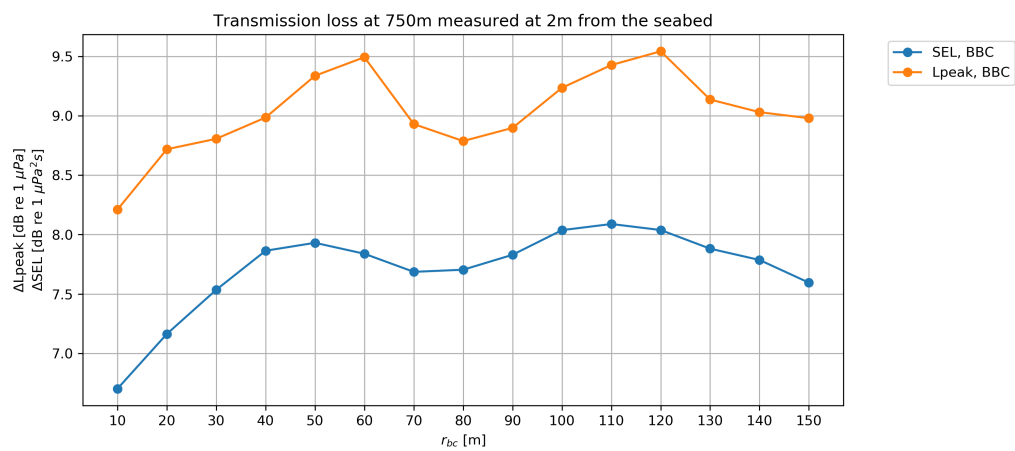
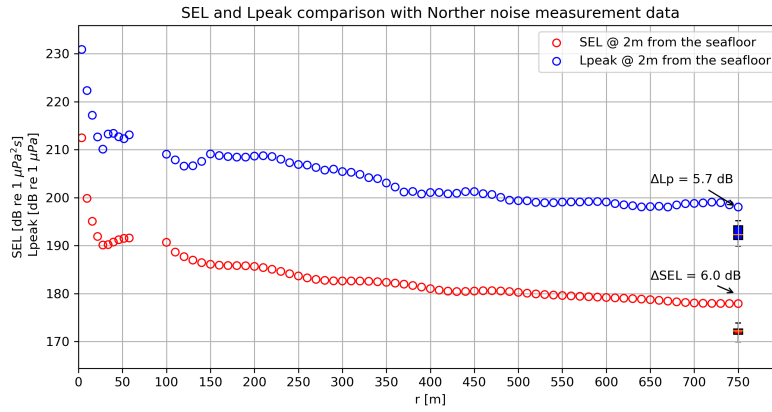
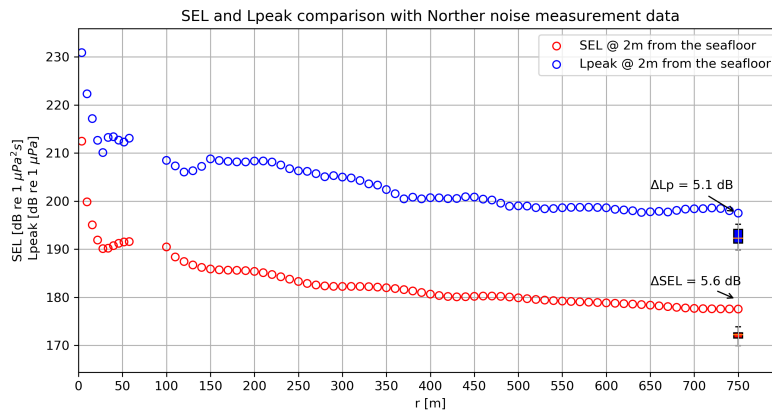


Figure B.6: BBC model

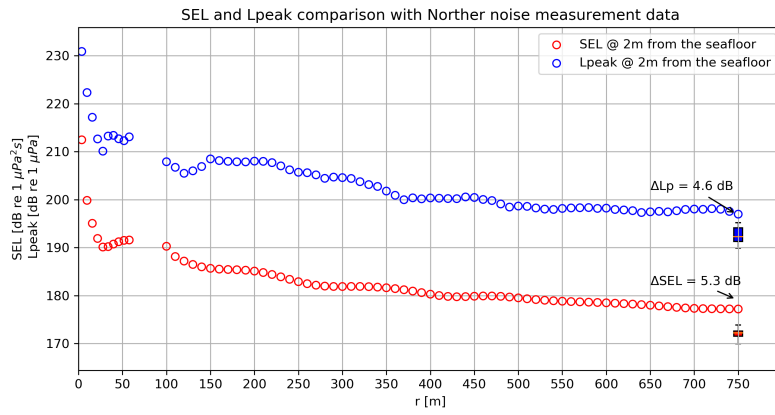
## C Sensitivity analysis for different bubble curtain configurations



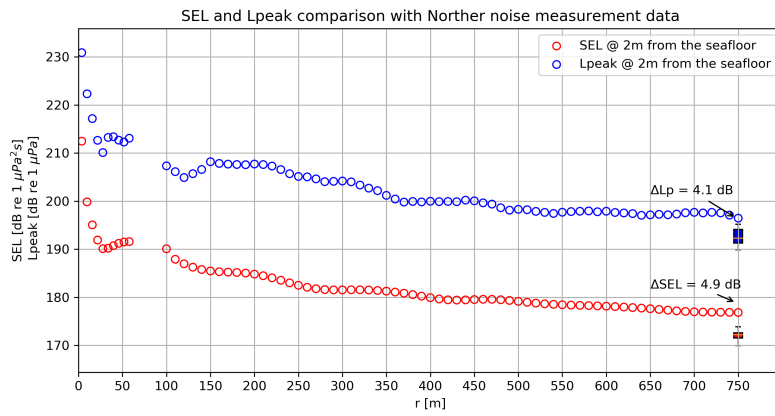
$$S_{min} = 0.03\text{m}, S_{max} = 0.1\text{m}$$



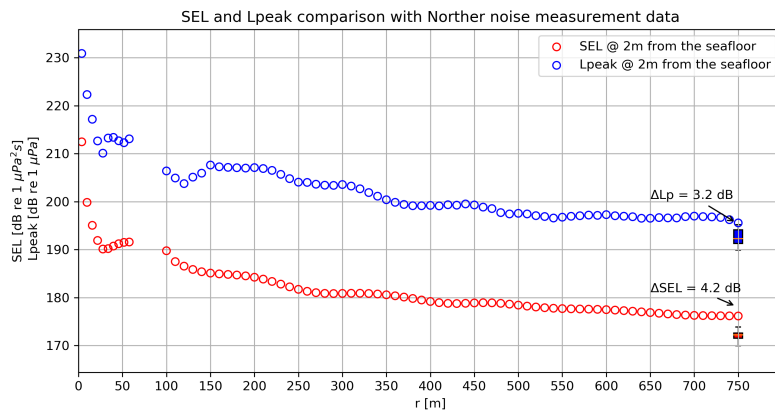
$$S_{min} = 0.04\text{m}, S_{max} = 0.1\text{m}$$



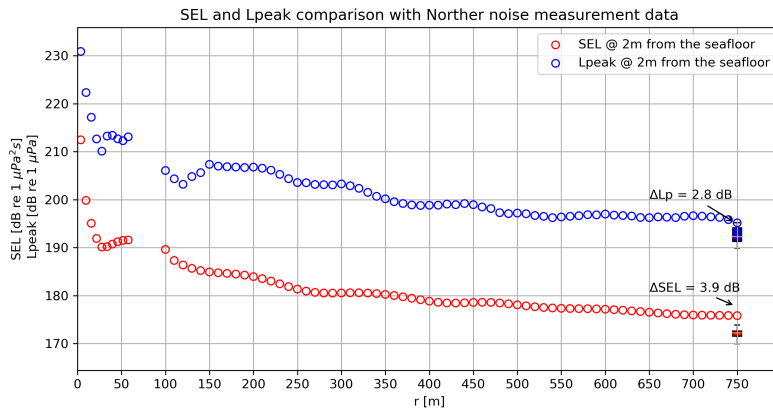
$$S_{min} = 0.05\text{m}, S_{max} = 0.1\text{m}$$



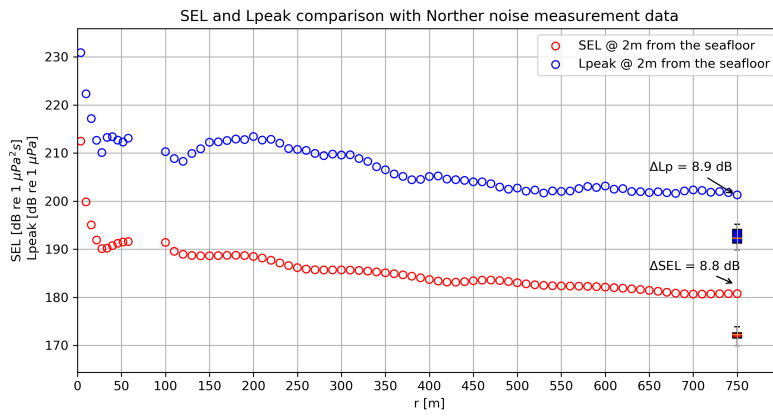
$$S_{min} = 0.06\text{m}, S_{max} = 0.1\text{m}$$



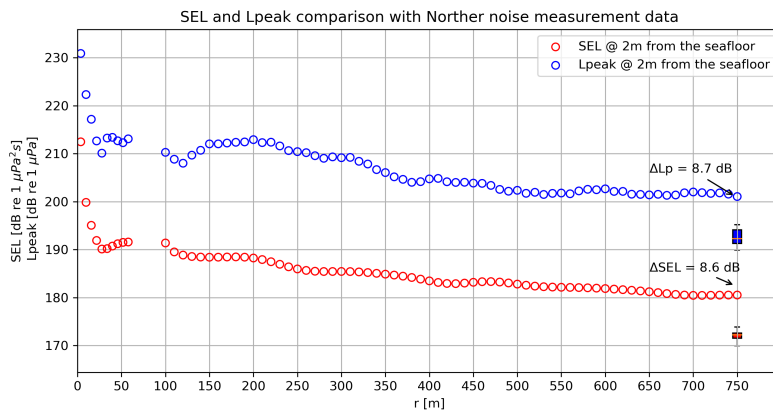
$$S_{min} = 0.08\text{m}, S_{max} = 0.1\text{m}$$



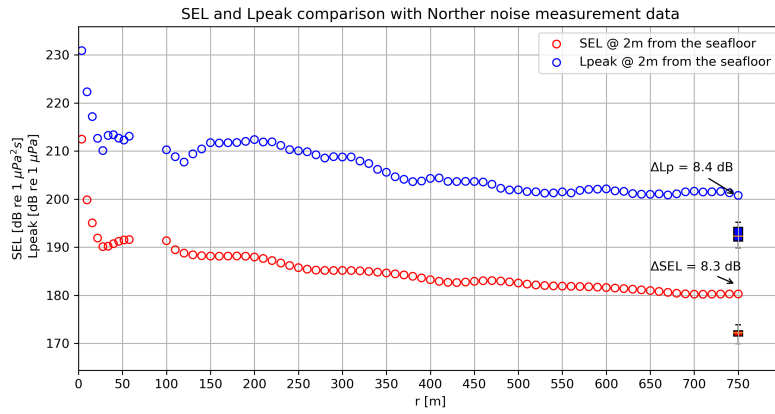
$$S_{min} = 0.09\text{m}, S_{max} = 0.1\text{m}$$



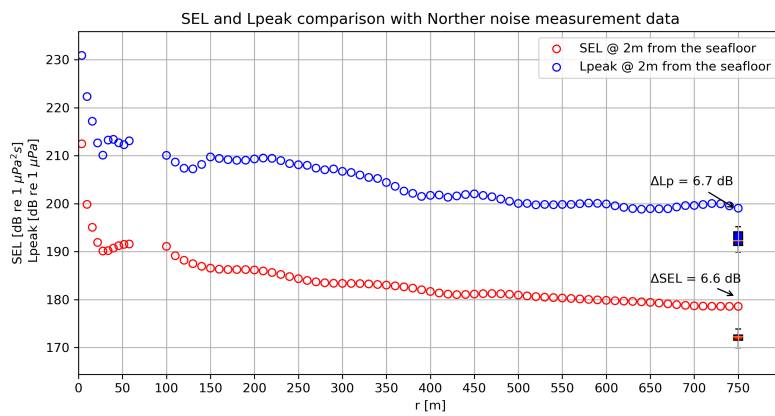
$$S_{min} = 0.01 \text{ m}, S_{max} = 0.02\text{m}$$



$$S_{min} = 0.01 \text{ m}, S_{max} = 0.03\text{m}$$



$$S_{min} = 0.01 \text{ m}, S_{max} = 0.04 \text{ m}$$



$$S_{min} = 0.01 \text{ m}, S_{max} = 0.1 \text{ m}$$

## D Notebooks

### Bubblecurtain package

<https://github.com/gjwglasbergen/Bubblecurtain>

